Extrusion-based 3D printed biodegradable porous iron

Putra, N. E.; Leeflang, M. A.; Minneboo, M.; Taheri, P.; Fratila-Apachitei, L. E.; Mol, J. M.C.; Zhou, J.; Zadpoor, A. A.

DOI
10.1016/j.actbio.2020.11.022

Publication date
2021

Document Version
Final published version

Published in
Acta Biomaterialia

Citation (APA)
Putra, N. E., Leeflang, M. A., Minneboo, M., Taheri, P., Fratila-Apachitei, L. E., Mol, J. M. C., Zhou, J., & Zadpoor, A. A. (2021). Extrusion-based 3D printed biodegradable porous iron. *Acta Biomaterialia*, *121*, 741-756. https://doi.org/10.1016/j.actbio.2020.11.022

Acta Biomaterialia 121 (2021) 741–756

Contents lists available at ScienceDirect

Acta Biomaterialia

journal homepage: www.elsevier.com/locate/actbio

Extrusion-based 3D printed biodegradable porous iron

N.E. Putra [a,*], M.A. Leeflang [a], M. Minneboo [a], P. Taheri [b], L.E. Fratila-Apachitei [a], J.M.C. Mol [b], J. Zhou [a], A.A. Zadpoor [a]

[a] Department of Biomechanical Engineering, Faculty of Mechanical, Maritime, and Materials Engineering, Delft University of Technology, Mekelweg 2, 2628 CD Delft, the Netherlands
[b] Department of Materials Science and Engineering, Faculty of Mechanical, Maritime, and Materials Engineering, Delft University of Technology, Mekelweg 2, 2628 CD Delft, the Netherlands

ARTICLE INFO

Article history:
Received 31 August 2020
Revised 10 November 2020
Accepted 16 November 2020
Available online 20 November 2020

Keywords:
3D printing
Material extrusion
Biodegradable
Iron
Scaffold
Bone substitution

ABSTRACT

Extrusion-based 3D printing followed by debinding and sintering is a powerful approach that allows for the fabrication of porous scaffolds from materials (or material combinations) that are otherwise very challenging to process using other additive manufacturing techniques. Iron is one of the materials that have been recently shown to be amenable to processing using this approach. Indeed, a fully interconnected porous design has the potential of resolving the fundamental issue regarding bulk iron, namely a very low rate of biodegradation. However, no extensive evaluation of the biodegradation behavior and properties of porous iron scaffolds made by extrusion-based 3D printing has been reported. Therefore, the *in vitro* biodegradation behavior, electrochemical response, evolution of mechanical properties along with biodegradation, and responses of an osteoblastic cell line to the 3D printed iron scaffolds were studied. An ink formulation, as well as matching 3D printing, debinding and sintering conditions, was developed to create iron scaffolds with a porosity of 67%, a pore interconnectivity of 96%, and a strut density of 89% after sintering. X-ray diffracometry confirmed the presence of the α-iron phase in the scaffolds without any residuals from the rest of the ink. Owing to the presence of geometrically designed macropores and random micropores in the struts, the *in vitro* corrosion rate of the scaffolds was much improved as compared to the bulk counterpart, with 7% mass loss after 28 days. The mechanical properties of the scaffolds remained in the range of those of trabecular bone despite 28 days of *in vitro* biodegradation. The direct culture of MC3T3-E1 preosteoblasts on the scaffolds led to a substantial reduction in living cell count, caused by a high concentration of iron ions, as revealed by the indirect assays. On the other hand, the ability of the cells to spread and form filopodia indicated the cytocompatibility of the corrosion products. Taken together, this study shows the great potential of extrusion-based 3D printed porous iron to be further developed as a biodegradable bone substituting biomaterial.

Statement of significance

3D printing techniques have been used to fabricate porous iron scaffolds for bone substitution. However, no extensive performance evaluation of porous iron made by extrusion-based 3D printing for bone substitution has ever been reported. Therefore, we comprehensively studied the *in vitro* biodegradation behavior, electrochemical characteristics, time-dependent mechanical properties, and cytocompatibility of porous iron scaffolds made by means of extrusion-based 3D printing. Our results showed that extrusion-based 3D printing could deliver porous iron scaffolds with enhanced biodegradability and bone-mimicking mechanical properties for potential application as biodegradable bone substitutes.

1. Introduction

Biodegradable metals and their alloys, including those based on magnesium, iron, and zinc, have been extensively studied to explore their potential as temporary bone substitutes [1,2]. Such

* Corresponding author.
E-mail address: n.e.putra@tudelft.nl (N.E. Putra).

https://doi.org/10.1016/j.actbio.2020.11.022

biodegradable biomaterials could alleviate the risk of prolonged inflammation associated with non-biodegradable metals that permanently remain at the implantation site [3]. Among biodegradable metallic materials, those based on iron enjoy the advantage of possessing substantially higher mechanical properties as compared to the magnesium- and zinc-based alternatives [4]. Those higher mechanical properties open up unique opportunities for adapting the mechanical properties of iron-based materials to those of the local bony tissue by introducing porous structures. The porous structure also has the added value of significantly enhancing the internal surface area of the implants to accelerate the biodegradation process of iron [5], which is otherwise extremely low.

Owing to its abundance in nature, ease of manufacturing, and high mechanical performance, iron-based materials have been extensively used as structural materials and potentially to be used as biodegradable materials for bone substitution [6]. Iron is an essential element in the human metabolism for transporting oxygen, mediating electron transfers, and accelerating enzyme reactions. It plays a role in immune function [7]. Moreover, the homeostasis of iron is essential for optimal bone regeneration [8]. Iron acts as a catalyst for the formation of reactive oxygen species (ROS) and an appropriate ROS level has been reported to regulate a pathway in osteoblast differentiation [9]. Adequate iron uptake *in vivo* can assist in the development of osteoblasts [10,11] and induce platelet activation [12], which is important for the initial healing stage of bone recovery. On the one hand, there is evidence that iron ions exhibit cytotoxicity when the rate of ion release exceeds a certain threshold [13]. On the other hand, long-term *in vivo* studies on iron-based bone substitutes have shown that the corrosion products are biocompatible [14,15]. It is important to note that the reported *in vivo* corrosion rates are extremely low with no significant changes in the mass of iron-based materials implanted in the bulk (after 52 weeks) [14] and foam (after 6 weeks) forms [15], which may lead to the longer-than-expected longevity of such iron-based implants (within a few years [16]). It is still an open research question whether the biocompatibility of iron-based materials remains favorable enough when their biodegradation rates are enhanced to match the rate of bone tissue healing. For implant applications, the ferromagnetic nature of iron, causing complications during magnetic resonance imaging (MRI), is another issue, which has been addressed by alloying with 28 wt% or more manganese to retain the austenite phase and change the alloy to be non-ferromagnetic [17].

To address the first issue, *i.e.*, too slow biodegradation of iron, recent research has been focused on developing new types of iron-based alloys [18,19], modifying the surface properties through sandblasting [20] and bio-functionalizing the surface using polymers [21-23] or bioceramics [24,25] to accelerate biodegradation. In addition, porous structures have been fabricated using various techniques, including both traditional techniques, such as electrodeposition [26], space holder method [27-31], powder molding onto porous template [32], and 3D printing techniques, such as binder/ink-jetting [33,34], material extrusion [35-39], and selective laser melting [40-43].

3D printing has recently emerged as the most promising approach to the fabrication of porous biodegradable metals [44,45]. Using this approach, tailor-made designs of biodegradable scaffolds can be realized to meet the specific requirements of various treatment conditions. Examples include tailor-made solutions to the treatment of critical bony defects and osteosynthesis as well as site-specific drug delivery for cancer patients [45]. 3D printed implants with a geometrically ordered pore network provide tissue-mimicking mechanical properties, facilitate osseointegration, and greatly increase the surface area to volume ratio, thereby increasing the rate of biodegradation. Extrusion-based 3D printing provides a straightforward approach to the *ex situ* fabrication of porous structures using metallic materials (or material mixtures), which would otherwise be challenging for other 3D printing techniques [46], such as powder bed fusion 3D printing processes [47,48].

In the last few years, 3D printing techniques, including material extrusion and selective laser melting (SLM), have been used to fabricate porous pure iron for bone substitution. Extrusion-based 3D-printed topologically ordered porous iron scaffolds with cubic unit cell (31% porosity) and hexagonal unit cell (60% porosity) have been evaluated in terms of their mechanical behavior [37-39]. The surface of lay-down patterned iron scaffolds has been biofunctionalized by applying hydroxyapatite coating for enhanced cell-material interaction [35]. A few in-depth studies on the material properties and biocompatibility of SLM porous iron have appeared in the literature too [40,41]. However, no extensive evaluation of porous iron made by extrusion-based 3D priFnting is available yet. We, therefore, studied the early-stage *in vitro* biodegradation behavior, electrochemical response, time-dependent mechanical properties, and cytocompatibility of lay-down patterned porous iron scaffolds made by means of extrusion-based 3D printing.

2. Materials and methods

2.1. Scaffold design, 3D printing, and post-processing

In this research, pure iron was chosen to understand the *in vitro* biodegradation behavior, electrochemical response, evolution of mechanical properties, and cytocompatibility of 3D printed scaffolds so as to build up a solid base, on which further endeavors could be made to addresss the other issues related to iron-based materials for biomedical applications, for example, by adding alloying elements or functional agents. Iron powder with 99.88 wt% purity, minor impurities (Cu, Ni, Mo, Al, Mn, Si, and Cr), and spherical particle morphology (Fig. 1a) produced through nitrogen gas atomization (Material Technology Innovations Co., Ltd., China) was sieved to reach a particle size distribution of D_{10} = 25.85 µm, D_{50} = 39.93 µm and D_{90} = 53.73 µm. A printable ink with iron powder loading was prepared by manually mixing the iron powder with a 5 wt% hydroxypropyl methylcellulose (hypromellose) polymer (M_w ~86 kDa, Sigma Aldrich, Germany) aqueous solution [35] at a mass ratio of 7:1 (corresponding to a volume ratio of 49:50), based on the preliminary experiments with different powder-to-binder (mass) ratios in order to choose a 3D printable ink. Then, the shear-thinning properties of the chosen ink were studied using an MCR302 rheometer (Anton Paar GmbH, Germany). In addition, thermogravimetric analysis (TGA) of hypromellose was performed using an SDT Q600 v20.9 thermogravimetric analyzer (TA Instruments, USA).

Porous iron scaffolds (10.5 mm in height and 10 mm in diameter) were designed with the GeSiM Robotics software (GeSiM Bioinstruments, Germany) to have a strut width of 410 µm, a strut spacing of 400 µm, a layer thickness of 328 µm, a designed porosity of 50%, and an initial design surface area of 40.4 cm^2 (Fig. 1b). The iron ink was extruded into 3D porous iron scaffolds through a 410 μm tapered nozzle tip using 3D BioScaffolder 3.2 (GeSiM Bio-instruments, Germany) with angles of 0° and 90° that interchanged every layer (Fig. 1c). The printing pressure and printing speed were set at 200 kPa and 5 mm/s, respectively. After 3D printing, the as-printed iron scaffolds were allowed to dry for at least 30 min in a desiccator, before being loaded into a tube furnace STF16/180 (Carbolite Gero Ltd., UK) under a highly pure argon atmosphere (purity: 99.9999%; inlet pressure: 1 bar) and held at 350 °C for 1 h for debinding and at 1200 °C for 6 h for sintering. Finally, the as-sintered iron scaffolds were ultrasonically cleaned

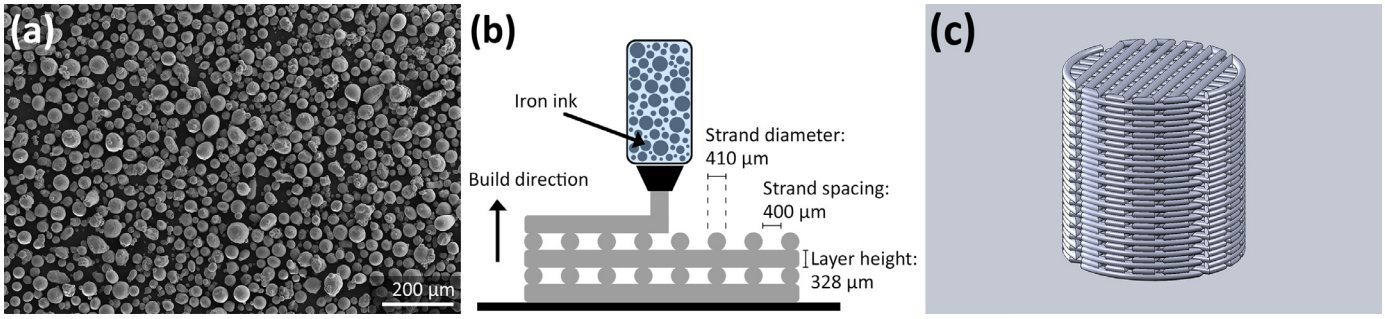

Fig. 1. The starting material, extrusion-based 3D printing, and scaffold design: (a) iron powder particle morphology, (b) an illustration of extrusion-based 3D printing, and (c) the scaffold with the 0° and 90° lay-down pattern design.

in isopropyl alcohol for 15 min prior to characterization and investigation.

2.2. Characterization of macrostructure and microstructure

The height and diameter of the porous iron scaffolds were measured before and after sintering to determine the shrinkage. The micro-architecture of the iron scaffolds was observed using a scanning electron microscope (SEM, JEOL JSM-IT100, Japan). From SEM images, the strut width, strut spacing, and layer thickness of the scaffolds were measured. The cross sections of the as-sintered iron scaffolds, after polishing up to 1 µm, were observed using SEM. The regions of interest on the cross section of the struts were defined and analyzed with color threshold in ImageJ (NIH, USA) to select the porous area. The solid fractions of the struts (X) were calculated based on the following equation:

$$X = \left(1 - \frac{Pore\ area}{Total\ area\ of\ ROI}\right) \times\ 100\% \quad (1)$$

Furthermore, the absolute porosities of the as-printed and as-sintered iron scaffolds were calculated, using the weighing method and Eqs. (2 and 3):

$$\varphi_p = \left(1 - \frac{m_p/\rho_{ink}}{V_{bulk}}\right) \times\ 100\% \quad (2)$$

$$\varphi_s = \left(1 - \frac{m_s/\rho_{iron}}{V_{bulk}}\right) \times\ 100\% \quad (3)$$

where φ_p and φ_s are, respectively, the absolute porosities of the as-printed and the as-sintered iron scaffolds [%], m is the mass of the as-printed or as-sintered iron scaffolds [g], V_{bulk} is the bulk volume of the scaffold [cm^3], ρ_{ink} is the density of the iron ink (*i.e.*, 4.41 g/cm^3), and ρ_{iron} is the theoretical density of pure iron (*i.e.*, 7.874 g/cm^3).

In addition, the interconnected porosity of the as-sintered iron scaffolds was assessed using the Archimedes' principle as described in the ASTM standard B963–13 [49]. The value was calculated using Eq. (4):

$$\varphi_i = \left(\frac{\rho_e}{\rho_o} \times \frac{m_{ao} - m_a}{m_{ao} - m_{eo}}\right) \times\ 100\% \quad (4)$$

where φ_i is the interconnected porosity of the as-sintered iron scaffolds [%], ρ_e is the density of ethanol (*i.e.*, 0.789 g/cm^3), ρ_o is the density of oil (*i.e.*, 0.919 g/cm^3), m_{ao} is the mass of the oil-impregnated iron scaffold weighed in air [g], m_a is the mass of the iron scaffold weighed in air [g], and m_{eo} is the mass of the oil-impregnated iron scaffold weighed in ethanol [g].

2.3. Phase identification

The phase composition of the as-sintered iron scaffolds was determined using an X-ray diffractometer (XRD, D8 Advance, Bruker, USA). XRD in the Bragg-Brentano geometry was equipped with a graphite monochromator and a Vantec position-sensitive detector that was set to work at 45 kV and 35 mA. A step size of 0.020° with a counting time of 10 s per step using Co Kα radiation was employed. The XRD pattern was evaluated using the Diffrac Suite.EVA v5.0 software (Bruker, USA) and the International Centre for Diffraction Data PDF-4 database.

2.4. *Static* in vitro *immersion tests*

Static *in vitro* immersion tests (up to 28 days, triplicates) were performed in the revised simulated body fluid (r-SBF) [50] using a cell culture incubator, under the following conditions: 5% CO_2, 2% O_2, relative humidity = 95%, temperature = 37 °C ± 0.5 °C. The solution volume-to-surface area ratio was 6.7 mL/cm^2 [51]. Before the tests, the samples were sterilized and the r-SBF solution was filtered using a 0.22 µm filter (Merck Millipore, Germany). The pH values were monitored during the immersion period using a pH electrode (InLab Expert Pro-ISM, METTLER TOLEDO, Switzerland). The concentrations of soluble calcium, phosphate and iron ions in the r-SBF solution were quantified using an inductively coupled plasma optical emission spectroscope (ICP-OES, iCAP 6500 Duo, Thermo Scientific, USA) after 1, 2, 7, 14, and 28 days of *in vitro* biodegradation. To determine the mass loss, the *in vitro* corrosion products were removed by immersing the as-corroded iron scaffolds at the abovementioned time points in a 50 vol% HCl solution (with a specific gravity of 1.19, Sigma Aldrich, Germany) containing 3.5 g/L hexamethylenetetramine (Sigma Aldrich, Germany) for 10 min, followed by ultrasonic cleaning in isopropyl alcohol for 15 min [52]. Subsequently, the samples were dried overnight in a desiccator and weighed using a balance with an accuracy of 0.1 mg. The cycle was repeated and the mass loss was plotted against the cleaning cycle to obtain the most accurate value, according to the ASTM standard G1–03 [52]. From the mass loss values, the average corrosion rate was determined based on the ASTM standard G31–72 [53] using Eq. (5):

$$CR_{immersion}\ [mm/year] = 8.76\ \times 10^4\ \times \frac{m}{A\ \times\ \rho\ \times\ t} \quad (5)$$

where m is the mass loss [g], A is the surface area of the scaffolds [cm^2] calculated based on the initial scaffold design value, ρ is the theoretical density of pure iron (*i.e.*, 7.874 g/cm^3), and t is the duration of *in vitro* immersion [h].

2.5. *Characterization of* in vitro *corrosion products*

The phases of the *in vitro* corrosion products of the scaffolds after 28 days of immersion were identified using XRD (D8 Advance, Bruker, USA). In addition, the morphologies of the *in vitro* corrosion products on the periphery of the iron scaffolds after 7, 14, and 28 days of continuous immersion were observed using SEM and their compositions were analyzed with an X-ray energy dispersive spectroscope (EDS, JEOL JSM-IT100, Japan). In addition to the periphery,

the scaffolds after 7, 14, and 28 days of continuous immersion were ground with SiC #2000, and the corrosion products in the center of the structure were characterized using SEM-EDS. Also, the fraction of the remaining base material (pure iron) after *in vitro* immersion at the selected time points was calculated using ImageJ (Eq. (1)).

2.6. Electrochemical measurements

To study the electrochemical corrosion behavior, iron scaffold specimens were carefully prepared by partial mounting them in thermoplastic acrylic resin and exposing them to r-SBF (pH=7.40, temperature = 37 ± 0.5 °C). The exposed surface area was calculated, based on the design value of the scaffold. Before the experiments, the mounted specimens were ultrasonically cleaned in isopropyl alcohol and then dried thoroughly. A three-electrode electrochemical system was configured, in which a graphite rod, an Ag/AgCl electrode, and the iron specimen, respectively, acted as the counter electrode, the reference electrode, and the working electrode. All the tests were carried out in triplicate using a Bio-Logic SP-200 potentiostat (Bio-Logic Science Instruments, France).

Before the electrochemical tests, the setup was allowed to reach a stable open circuit potential (OCP) for 1 h. The linear polarization resistance (LPR) tests of the iron specimens at different time points up to 28 days were carried out from −25 to +25 mV *versus* OCP at a scan rate of 0.167 mV/s. Consecutively, the electrochemical impedance spectroscopy (EIS) tests of the iron specimens at different time points up to 28 days were conducted using a sine amplitude of 10 mV *versus* OCP at a frequency scan between 100 kHz to 10 mHz. Moreover, potentiodynamic polarization (PDP) tests were performed on the specimens after 1 day and 28 days of immersion, with polarization between −300 to +500 mV *versus* OCP at a scan rate of 0.5 mV/s. From the PDP results, the corrosion rates were calculated according to the ASTM standard G102–89 [54] and using Eq. (6):

$$CR_{electrochemical}\ [\mathrm{mm/year}] = 3.27 \times 10^{-3} \times EW \times \frac{i_{corr}}{\rho} \qquad (6)$$

where EW is the equivalent weight of iron (valence 2), i_{corr} is the current density [μA/cm^2], and ρ is the theoretical density of pure iron [g/cm^3].

2.7. Uniaxial compression tests

An Instron universal testing machine (ElectroPuls E10000, Germany) with a 10 kN load cell was used to evaluate the compressive mechanical properties of the as-sintered iron scaffolds as well as the specimens retrieved after 1, 2, 7, 14 and 28 days of *in vitro* immersion. The tests were performed at a crosshead speed of 3 mm/min. The mechanical properties of the porous iron scaffolds, including the quasielastic gradient (referred as elastic modulus) and yield strength, were obtained following the ISO standard 13,314 [55]. The slope of the first linear region in the stress-strain graph was defined as the elastic modulus. A parallel line to the initial linear elastic region, offset by 0.2% strain, was drawn and the stress value at the intersection with the stress-strain curve was determined as the yield strength. The tests were performed in triplicate. The average values with standard deviations are reported hereafter.

2.8. Cytocompatibility evaluation

2.8.1. Pre-culture of MC3T3-E1 cells and the preparation of iron extract media

Preosteoblasts MC3T3-E1 (Sigma Aldrich, Germany) were precultured for 7 days in α-minimum essential medium (α-MEM, Thermo Fisher Scientific, USA) without ascorbic acid and supplemented with 10% fetal bovine serum (FBS, Thermo Fisher Scientific, USA) and 1% penicillin/streptomycin (p/s, Thermo Fisher Scientific, USA). α-MEM without ascorbic acid was used to maintain the cells in the preosteoblastic state. The cells were incubated at 37 °C in a humidified atmosphere with 5% CO_2 and 2% O_2 (relative humidity = 95%). The culture medium was refreshed every 2 to 3 days.

The iron extract culture media were prepared by immersing the sterilized porous iron scaffolds (10.25 mm in height and 9.75 mm in diameter) in α-MEM (without ascorbic acid, but with 10% FBS, 1% p/s) for 72 h at 37 °C in a 5% CO_2 and 2% O_2 atmosphere with 95% relative humidity [56]. The specimen-to-medium ratio was 5 cm^2/mL, in which the surface area of the scaffolds was calculated based on the design value. Thereafter, the supernatant was collected, filtered, and diluted into 75%, 50%, 25%, and 10% from the original concentration. Furthermore, the iron ion concentration in the original (100%) iron extract media was quantified using ICP-OES (iCAP 6500 Duo, Thermo Scientific, USA). All media were kept at 4 °C prior to cell tests.

2.8.2. Indirect cytotoxicity tests

To evaluate the indirect cytocompatibility of the iron scaffolds, the PrestoBlue assay (Thermo Fisher Scientific, USA) was performed. The MC3T3-E1 preosteoblasts (1×10^4 cells) were cultured in 200 μL of 100%, 75%, 50%, 25% and 10% iron extract media using 48-well plates. The same number of cells was cultured in the original α-MEM (without ascorbic acid, but with 10% FBS, 1% p/s) as the negative control. After 1, 3, and 7 days of culture, the iron extract media were replaced with 200 μL fresh pure α-MEM (without ascorbic acid, but with 10% FBS, 1% p/s) to prevent the interference of iron ions with the assay. Consecutively, 20 μL of PrestoBlue reagents (Thermo Fisher Scientific, USA) were added, and the specimens were incubated at 37 °C for 1 h. Afterwards, the absorbance values were measured with a Victor X4 Wallac plate reader (PerkinElmer, USA) at a wavelength of 530 - 590 nm. The tests were performed in triplicate. The average metabolic activity of the cells is reported as a percentage of the negative control, calculated using Eq. (7):

$$Metabolic\ activity\ [\%] = \frac{Absorbance\ (specimen)}{Absorbance\ (negative\ control)} \times 100 \qquad (7)$$

To observe the morphology of the preosteoblasts grown in the iron extract media, the cytoskeleton and nucleus of the cells were stained using rhodamine phalloidin and 4′,6-diamidino-2-phenylindole (DAPI) dyes, respectively. The MC3T3-E1 preosteoblasts (1×10^4 cells) were cultured for 3 days on 48-well glass disks in 200 μL of iron extract media. The same number of cells was cultured in the original α-MEM (without ascorbic acid, but with 10% FBS, 1% p/s) as the negative control. After culture, the specimens were washed with PBS (Thermo Fisher Scientific, USA), fixed using 4% formaldehyde (Sigma Aldrich, Germany) for 15 min at room temperature, then washed with PBS, and permeabilized with 0.5% triton/PBS (Sigma Aldrich, Germany) at 4 °C for 5 min. Then, 1% bovine serum albumin/PBS (BSA, Sigma Aldrich, Germany) was added per well and followed by incubation for 5 min. Consecutively, 1:1000 rhodamine phalloidin (Thermo Fisher Scientific, USA) in 1% BSA/PBS was added per well, followed by 1 h incubation at 37 °C. Afterwards, the specimens were rinsed in 0.5% tween/PBS (Sigma Aldrich, Germany) and washed with PBS. Finally, the specimens were mounted on a glass slide with Prolong gold (Life Technologies, USA), containing the DAPI dye. Thereafter, the morphology of the cells cultured in different iron extracts was observed using a fluorescence microscope (ZOE cell imager, Bio-Rad, USA). From staining images, the number of cells and the cell

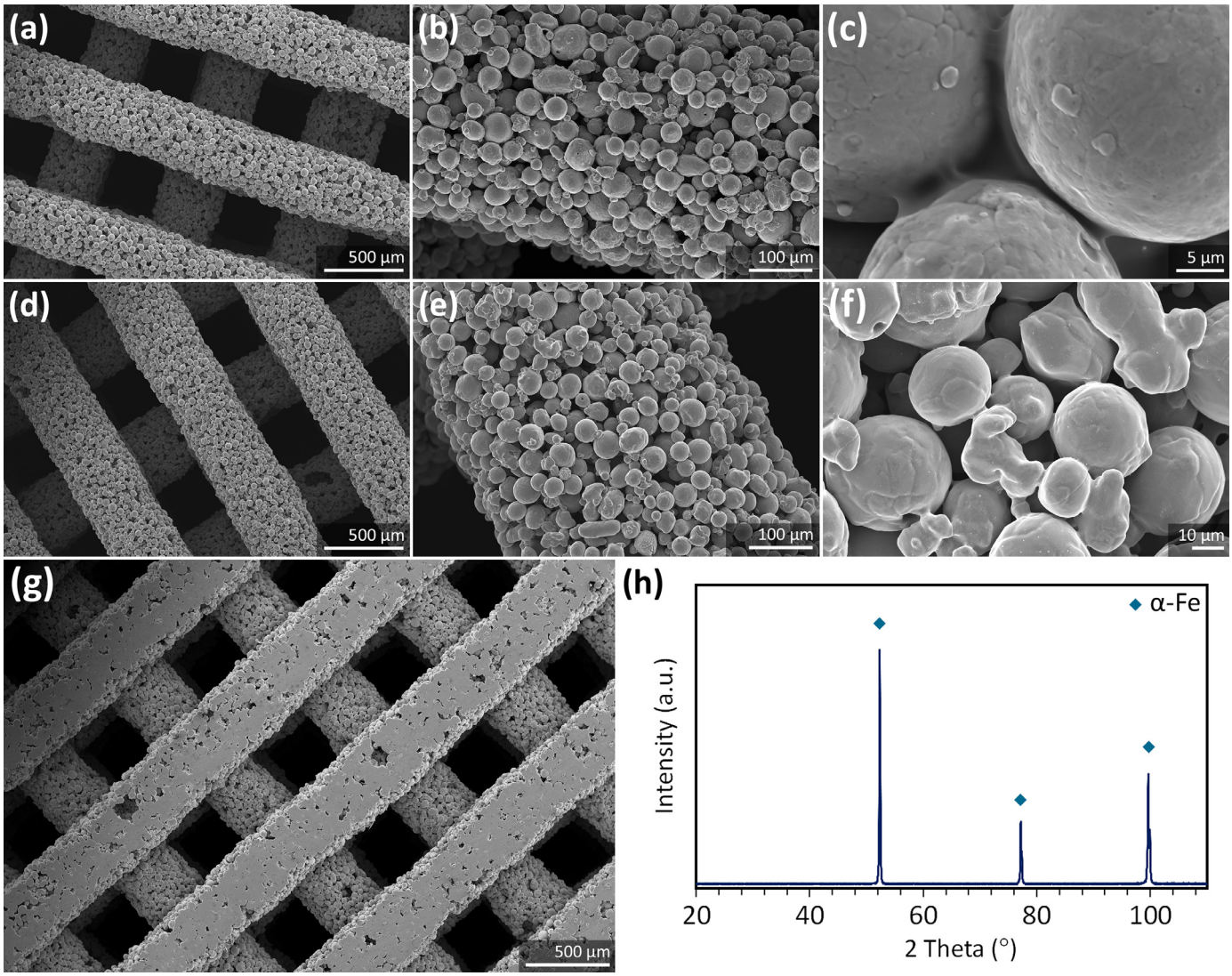

Fig. 2. Morphology and phase composition of the porous iron scaffolds: SEM images of (a, b, c) the as-printed iron scaffolds and (d, e, f) the as-sintered iron scaffolds at different magnifications, (g) the cross-section of the polished struts, and (h) the XRD pattern of the scaffolds after sintering. (For interpretation of the references to colour in this figure legend, the reader is referred to the web version of this article.)

spreading area were determined by counting the nucleus of the cells using ImageJ (NIH, USA).

2.8.3. Direct cytotoxicity tests

To evaluate the direct cytocompatibility of the iron scaffolds, the Trypan blue cell counting assay was performed. First, the porous iron scaffolds (10.25 mm in height and 9.75 mm in diameter) were pre-immersed in α-MEM (without ascorbic acid, but with 10% FBS, 1% p/s) for 5 min and placed in the 6-well plate. After that, the MC3T3-E1 preosteoblasts (1×10^6 cells per specimen) were pipetted into the porous iron scaffolds. Subsequently, 10 mL of α-MEM was added per well to immerse the scaffold. The same number of cells was cultured for all experimental groups. For every time point, the tests were performed in triplicate. After 1, 3, and 7 days of culture, the cells were trypsinized from the scaffolds and the well plates and then suspended. 10 µL of each cell suspension was mixed with 10 µL of trypan blue dye (Bio-Rad, USA) and subsequently pipetted into a dual-chamber cell counting slide. The number of living cells was counted using an automated cell counter (TC20, Bio-Rad, USA). The average number of living cells with standard deviations are reported.

In addition, to observe the distribution and morphology of MC3T3-E1 cells seeded on the porous iron scaffolds, a live/dead staining assay was performed, followed by SEM imaging. The MC3T3-E1 preosteoblasts (2×10^5 cells per specimen) were seeded on the iron scaffolds (2.05 mm in height and 9.75 mm in diameter) and cultured in 2 mL α-MEM (without ascorbic acid, but with 10% FBS, 1% p/s). After 3 days of culture, the specimens were washed with PBS and immersed in PBS containing 2 µL/mL of calcein (Thermo Fisher Scientific, USA) and 1.5 µL/mL of ethidium homodimer-1 (Thermo Fisher Scientific, USA) for 30 min in the dark at room temperature. Thereafter, the live and dead cells on the iron scaffolds were observed using a fluorescence microscope (ZOE cell imager, Bio-Rad, USA). Furthermore, SEM imaging of cell morphologies on the iron scaffolds was performed. Briefly, after 3 days of culture, the specimens were washed in PBS, fixed with 4% formaldehyde (Sigma Aldrich, Germany) for 20 min, followed by dehydration stages in 30, 50, 70, and 100% ethanol for 10 min each, and they were further preserved using hexamethyldisilazane (Sigma Aldrich, Germany) for 30 min. The specimens were dried for 2 h prior to SEM imaging.

2.9. Statistical analysis

All values are expressed as mean ± standard deviation. The statistical analysis of the PrestoBlue results was performed with two-

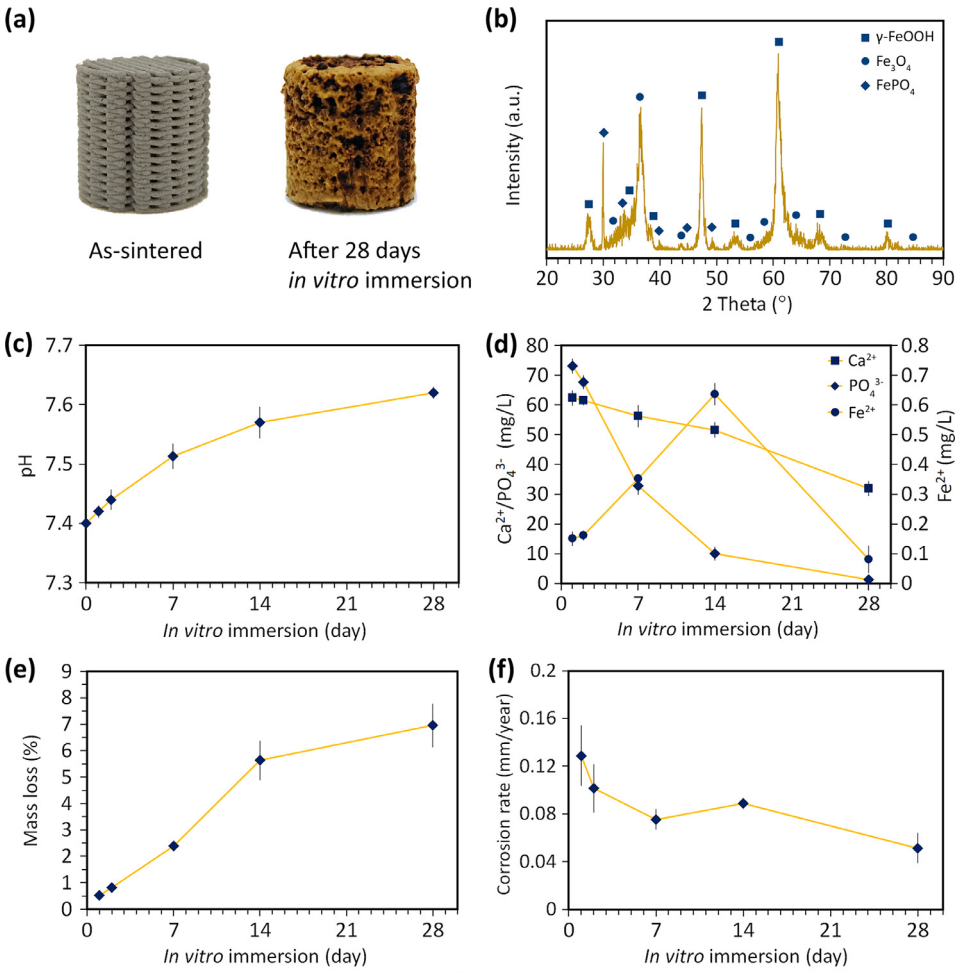

Fig. 3. *In vitro* corrosion characteristics of the porous iron scaffolds: (a) visual observation of the scaffolds before and after 28 days of immersion, (b) XRD pattern of the corrosion products on the iron scaffolds at day 28, (c) pH values of the r-SBF solution, (d) the Ca, PO_4, and Fe ion concentrations in the r-SBF throughout the immersion period, (e) the mass loss percentages, and (f) the corrosion rate of the scaffolds.

Table 1
Characteristics of the porous iron scaffolds made by extrusion-based 3D printing.

Sample group	Strut width (μm)	Strut spacing (μm)	Layer thickness (μm)	Absolute porosity (%)	Interconnected porosity (%)
Design	410	400	320	50	–
As-printed iron	420.3 ± 5.5	390.6 ± 5.6	327.4 ± 4.4	47 ± 4	–
As-sintered iron	411.2 ± 5.9	398.9 ± 5.7	320.2 ± 3.7	67 ± 2	65 ± 1

way ANOVA followed by the Tukey *post hoc* test. For the direct cytocompatibility cell count results, statistical analysis was conducted with one-way ANOVA, followed by the Tukey *post hoc* test.

3. Results

3.1. Structural characteristics of the porous iron scaffolds

The porous iron scaffolds exhibited a free-standing characteristic, where the struts bridged above the underlying layers (Fig. 2a). Sufficient powder loading in the ink (Fig. 2b) and strong bond between powder particles and binder (Fig. 2c) allowed the scaffolds with a high aspect ratio to be built and to stay intact without distortions or shrinkage after 3D printing. The as-printed specimens had an absolute porosity of 47 ± 4%, with an average strut width of 420.3 ± 5.5 μm, and a strut spacing of 390.6 ± 5.6 μm (Table 1).

After sintering (Fig. 2d-e), the dimensions of the specimens were slightly reduced by 2.3 ± 0.2% (height) and 2.5 ± 0.2% (diameter). The strut width changed to 411.2 ± 5.9 μm while the strut spacing became 398.9 ± 5.7 μm (Table 1). At the periphery of the scaffolds, the fusion of iron particles with evident open pores between the necks of iron powder particles could be observed (Fig. 2f). On the cross section, a partially sintered microstructure with pores ranging between 26 and 135 μm inside the struts was observed (Fig. 2g). Despite the presence of micropores, the average solid fraction of the struts was high (*i.e.*, 89 ± 4%). The absolute porosity of the as-sintered specimens was 67 ± 2% and the total interconnected porosity was 65 ± 1%, corresponding to a pore interconnectivity of 96%. Based on the XRD analysis, the as-sintered iron scaffolds only contained the α-iron phase (Fig. 2h) without any detectable binder residues.

3.2. In vitro *corrosion behavior and the corrosion products*

After 28 days of static *in vitro* immersion, a thick brown corrosion layer almost entirely covered the periphery of the specimens (Fig. 3a). The corrosion products were mostly composed of iron oxide hydroxide (γ-FeOOH), magnetite (Fe_3O_4), and iron phosphate

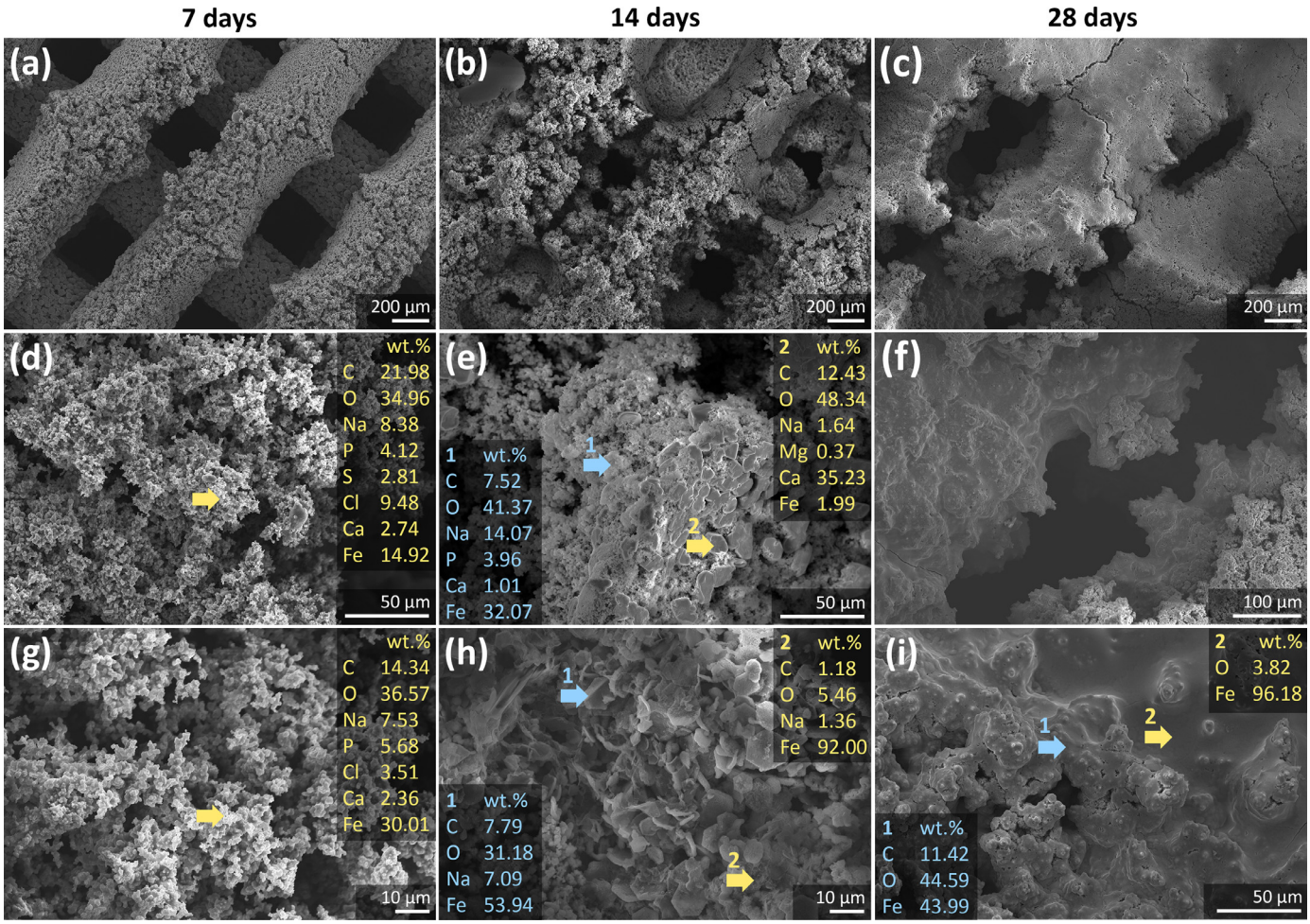

Fig. 4. Morphology and chemical compositions of the *in vitro* corrosion products at the periphery of the porous iron scaffolds: SEM and EDS point analysis of the corrosion products after (a, d, g) 7 days, (b, e, h) 14 days, and (c, f, i) 28 days of immersion. The arrow and number indicate where the EDS point analysis was performed and the corresponding elemental composition, respectively.

($FePO_4$) (Fig. 3b). The immersion tests performed with 5% CO_2 and 2% O_2 slightly increased the pH of the r-SBF solution to 7.62 at day 28 (Fig. 3c).

Throughout the *in vitro* immersion tests, the release of iron ions to the r-SBF solution remained < 1 ppm (Fig. 3d). The concentration of iron ions increased from 0.15 ppm to 0.64 ppm in the first 14 days of immersion and then decreased to 0.08 ppm (at day 28). On the other hand, the concentrations of calcium and phosphate ions in the r-SBF solution continuously decreased over time (Fig. 3d). A much higher rate of reduction in the concentration of the phosphate ion in the solution was observed in the first 14 days of immersion (Fig. 3d), while a slightly higher precipitation rate of calcium ions on the specimens was noticed between days 14 and 28. The mass of the iron scaffolds was reduced by 7 ± 1% after 28 days of immersion (Fig. 3e). The average *in vitro* corrosion rate after 1 day of immersion was 0.28 ± 0.05 mg/cm^2/day, but declined to 0.11 ± 0.01 mg/cm^2/day after 28 days. According to the ASTM standard G31–72 [53], the average corrosion rates after 1 day and 28 days of immersion could be converted into 0.13 ± 0.03 and 0.05 ± 0.01 mm/year, respectively (Fig. 3f).

After 7 days of immersion, loose corrosion products surrounded the struts of the scaffolds (Fig. 4a). Fine granules of the corrosion products, which were rich in iron, oxygen, and carbon and contained sodium, calcium, phosphorus, and chlorine, were identified (Fig. 4d and g). After 14 days of immersion, the thickness of the corrosion layer increased and almost filled the macropores of the iron scaffolds (Fig. 4b). The morphologies of the corrosion products consisted of a mixture of fine and coarse granules (Fig. 4e) and a flake-like structure (Fig. 4h). The composition of the finer granules was similar to the one seen after 7 days of immersion (Fig. 4e, EDS 1), whereas the coarser granules mainly contained calcium, oxygen, and carbon with trace amounts of iron, sodium, and magnesium (Fig. 4e, EDS 2). In the flake-like corrosion products, iron and oxygen were dominant, but carbon and sodium existed too (Fig. 4h). After 28 days of immersion, the corrosion products developed into a more compact structure (Fig. 4c, f). The dense corrosion layer was composed of iron, carbon, and oxygen (Fig. 4i, EDS 1) or iron and oxygen (Fig. 4i, EDS 2).

In addition to the periphery, the corrosion products were also formed in the interconnected pore network of the struts of the scaffolds (Fig. 5a-c). The corrosion products in the micropores were predominantly composed of oxygen with traces of iron, calcium, and carbon (Fig. 5d-e). Moreover, two other types of corrosion products were identified in the center of the scaffolds after 28 days of immersion (Fig. 5f-g). One type, on the strut surface, had a flake-like morphology and contained iron, oxygen, and carbon (Fig. 5g, EDS 1). The other type had a crystal-like spherical morphology and contained iron, oxygen, carbon, and calcium (Fig. 5g, EDS 2). As the biodegradation progressed, the pure iron present in the scaffolds was gradually consumed. The pure iron fraction in the struts reduced from 89 ± 4% before the start of the immersion test to 87 ± 2%, 79 ± 2%, and 79 ± 2% after 7, 14, and 28 days of immersion, respectively (Fig. 5h).

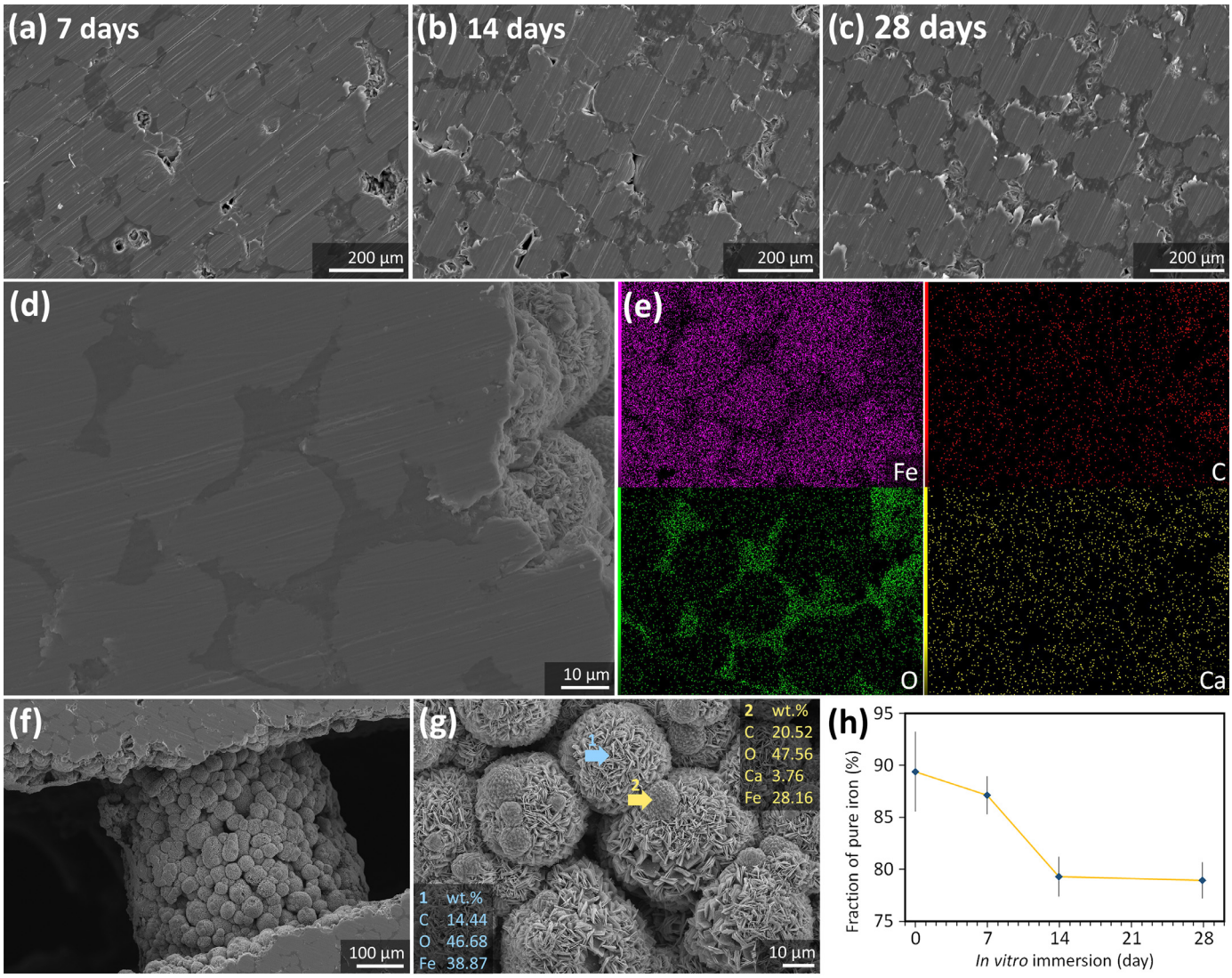

Fig. 5. Morphology and chemical compositions of the *in vitro* corrosion products in the center of the porous iron scaffolds: the cross section of the scaffolds after (a) 7, (b) 14, and (c) 28 days of immersion, (d) a magnified view of the corrosion products at day 28 in the pore network and (e) the elemental mapping, (f) corrosion products on the struts after 28 days of immersion and (g) the enlarged view of the corrosion products with EDS point analysis, and (h) reductions in the pure iron fraction in the struts during the immersion period. The arrow and number indicate where the EDS point analysis was performed and the corresponding elemental composition, respectively. (For interpretation of the references to colour in this figure legend, the reader is referred to the web version of this article.)

3.3. Electrochemical response

According to the PDP curves (Figure S2a), the corrosion potential of the iron scaffolds shifted from -781 ± 22 mV after 1 day of immersion to -676 ± 17 mV after 28 days of immersion. At the same time points, the corrosion current densities decreased from 8.0 ± 0.3 µA/cm^2 to 3.5 ± 0.6 µA/cm^2 (Figure S2a). According to the ASTM standard G102–89 [54], the corrosion rate, based on the current densities, were calculated to be 0.09 and 0.04 mm/year after 1 day and 28 days of immersion, respectively. The results were quite close to the values obtained from the *in vitro* immersion tests in the cell culture incubator. Moreover, the polarization resistance of the iron scaffolds was 3.3 ± 0.6 kΩ.cm^2 after 1 day of immersion. It increased to 8.4 ± 1.4 kΩ.cm^2 at day 7 and reduced to 4.9 ± 0.7 kΩ.cm^2 at day 9 of immersion (Figure S2b). From day 9, the value continuously increased with an average rate of 0.35 kΩ.cm^2 per day until day 21, became 9.1 ± 2.1 kΩ.cm^2. At day 28 of immersion, the polarization resistance was 26.7 ± 6.5 kΩ.cm^2.

The Bode plots of the impedance against frequency (Fig. 6a, S2c) generally showed increases in the impedance modulus for low (*e.g.*, 0.01 Hz) and medium (*e.g.*, 10 Hz) frequencies for the entire duration of the immersion tests. The Bode plots impedance at 0.01 Hz after 1 day and 28 days of immersion were 2.8 ± 0.6 kΩ.cm^2 and 33.1 ± 2.4 kΩ.cm^2, respectively. At these time points, the Bode impedance at 10 Hz were 0.3 ± 0.1 kΩ.cm^2 and 11.4 ± 1.4 kΩ.cm^2, respectively. In the Bode plot of phase angle against frequency (Fig. 6b), the phase angle values at high frequencies (*e.g.*, 10 kHz) decreased from −1.3° after 1 day to −53.9° after 28 days of immersion. In the case of low frequencies (*e.g.*, 0.1 Hz), however, the phase angle values moved towards more positive values, showing a shift in the peak of the plot from a higher frequency to a lower frequency throughout the immersion time (Fig. 6b).

The Nyquist plots displayed three different types of spectra throughout the immersion test. The Nyquist plot after 1 day of immersion showed a single capacitive arc (Fig. 6c). After 7 days of immersion, the Nyquist plot showed a larger curve than that of the 1-day immersion plot (Fig. 6c). From 9 until 24 days of immersion, the Nyquist plots exhibited a two-semicircle continuous arc that began with a smaller semicircle at a higher frequency and continued with an inclined slope forming a second larger curve at

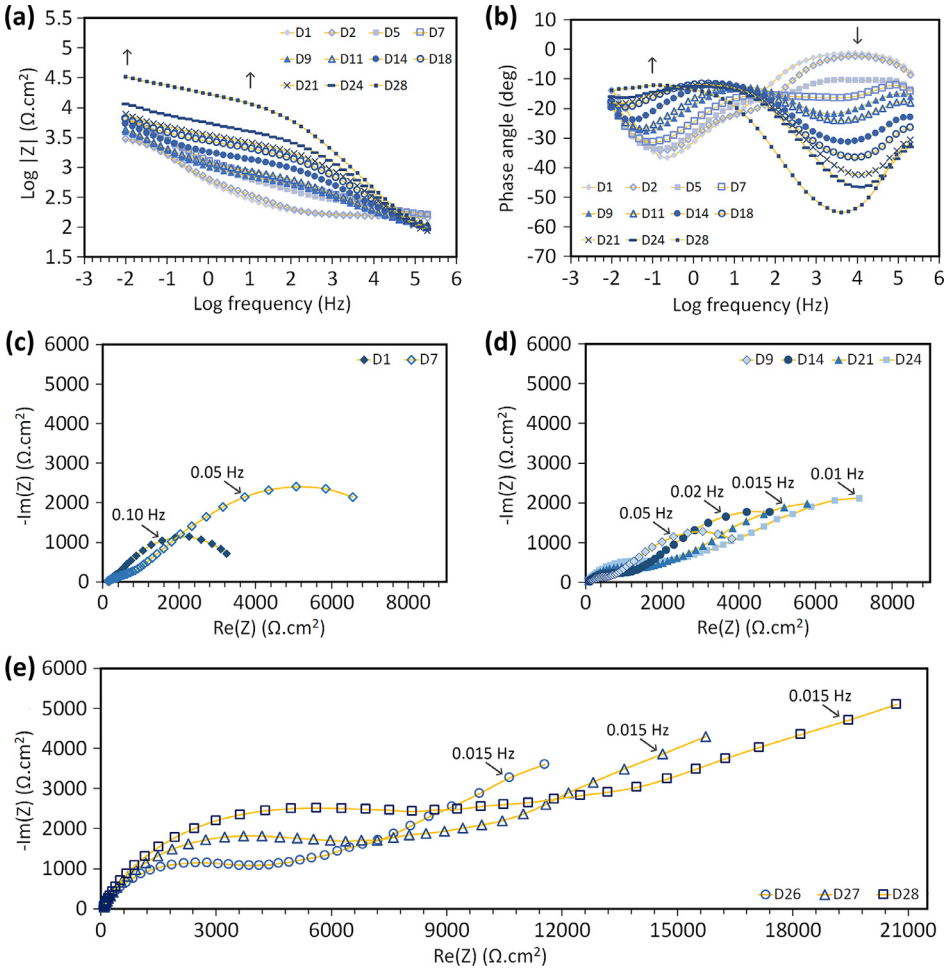

Fig. 6. Electrochemical impedance spectroscopy of the porous iron scaffolds: the Bode plots of (a) impedance modulus and (b) phase angle against frequency for up to 28 days of immersion, Nyquist spectra (c) after 1 and 7 days, (d) 9, 14, 21, and 24 days, and (e) 26 to 28 days of immersion. The arrows in Bode plots indicate the change in the impedance and phase angle values with time for a specific frequency.

a lower frequency (Fig. 6d). In addition to the increase in the diameter of the semicircle arc over time, the angle of the inclined slope decreased as corrosion progressed (Fig. 6d). After 28 days of immersion, the semicircle at the high-frequency region was larger and extended with a moderately inclined straight line for the lower frequencies (Fig. 6e). fail

3.4. Mechanical properties

The uniaxial compressive stress-strain curves of the porous iron scaffolds (Fig. 7a) began with a linear elastic region, followed by a trend resembling strain-hardening during the plastic deformation stage until specimen failure. The as-sintered iron scaffolds exhibited a yield strength of 7.2 ± 0.4 MPa and an elastic modulus of 0.6 ± 0.1 GPa. Over the *in vitro* immersion period of 28 days, the yield strength of the scaffolds increased to 10.6 ± 0.2 MPa after 2 days of immersion and slightly reduced to 9.4 ± 0.9 MPa after 28 days of immersion (Fig. 7b). Likewise, the elastic modulus increased to 0.6 ± 0.1 GPa after 2 days of immersion and stabilized at an average value of 0.7 ± 0.2 GPa after 28 days of immersion (Fig. 7b). On the other hand, the ultimate strength remarkably dropped from 96 ± 6 MPa to 32 ± 2 MPa after 7 days of immersion. Then, it further decreased to 19 ± 7 MPa after 28 days of immersion (Fig. 7c). Moreover, the iron scaffolds became less ductile after the immersion tests and a notable decline in strain at failure from 53 ± 3% to 31 ± 3% was observed after 7 days of immersion. The strain at failure further decreased to 13 ± 3% after 28 days of immersion (Fig. 7c).

3.5. In vitro *cytotoxicity against MC3T3-E1 preosteoblasts*

The 100% iron extract medium contained 120.4 ± 3.7 ppm of iron ions. The exposure to the 100% iron extract medium resulted in instant cytotoxicity, with 25.6 ± 4.8% metabolic activity remaining after 24 h and almost no metabolically active cells after 7 days of culture (Fig. 8a). After the iron extract was diluted to 75% of its original, a metabolic activity of 73.3 ± 9.3% was detected after 24 h culture. However, the trend of decreased activity with culture time (*i.e.*, 33.3 ± 5.9% after 7 days) remained unchanged. When the iron extract medium was further diluted to ≤ 50%, the growth of the preosteoblasts was only slightly inhibited, as indicated by the high metabolic activity (> 80%) even after 7 days of culture (Fig. 8a).

From the stained samples, the cell counts from 100%, 75%, and 50% iron extracts were 133 ± 16 (Fig. 8c), 190 ± 63 (Fig. 8d), and 753 ± 59 (Fig. 8e), respectively. More cells were observed when they were cultured in a lower-concentration iron extract medium. Furthermore, the individual stress fibers and filopodia of each cell cultured in the 100% and 75% iron extract remained recognizable (Fig. 8c-d). The preosteoblasts in the 75% iron extract exhibited a polygonal shape and were more outspread (2580.5 ± 247.5 μm^2 per cell) than the cells grown in the 100% iron extract (1736.4 ± 209.9 μm^2 per cell).

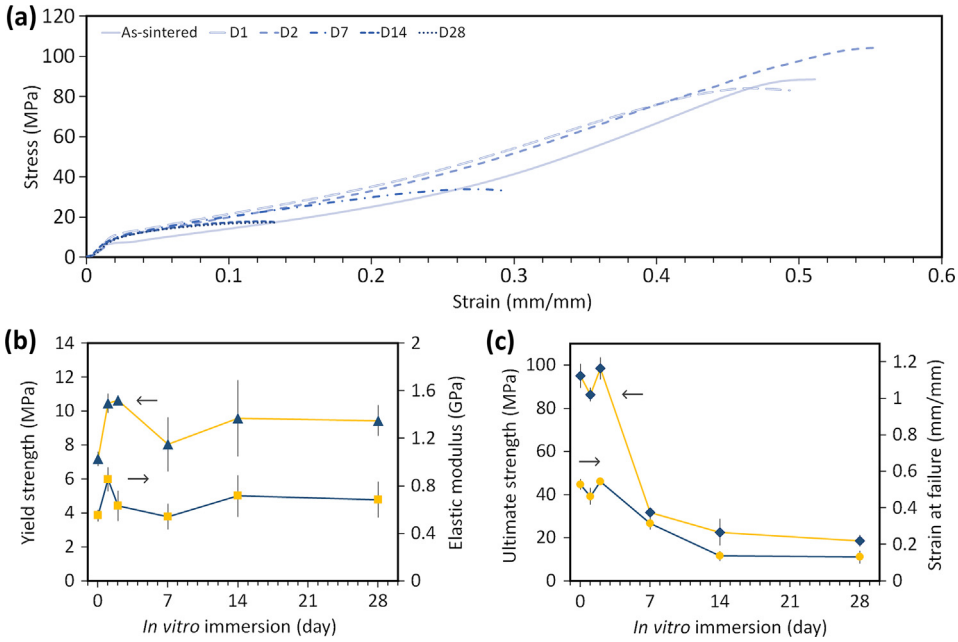

Fig. 7. Mechanical properties of the porous iron scaffolds: (a) compressive stress-strain curves, (b) the yield strength and elastic modulus, and (c) the ultimate strength and strain at failure of the scaffolds before and after *in vitro* immersion for up to 28 days.

The direct seeding of the preosteoblasts on the porous iron scaffolds resulted in a reduction in the living cell count after 24 h of culture (*i.e.*, 2.8 ± 0.3 (× 10^5) cells) (Fig. 8b). The viable cells continuously declined to 5.6 ± 1.5 (× 10^4) cells, after 3 days of culture ($p < 0.001$). Interestingly, at day 7 of culture, the viable cell count slightly increased to 6.9 ± 2.0 (× 10^4) cells (statistically not significant). Although it was challenging to quantify the live/dead staining results, a number of viable (green) preosteoblasts were detectable on the iron scaffolds (Fig. 8f-h). More importantly, the stained preosteoblasts showed a homogenous distribution over the struts of the porous iron scaffolds (Fig. 8f-h), indicating a good cell seeding efficiency in the direct assays. Furthermore, on the SEM images, the surviving cells were identified with extended filopodia in the porous structure of the scaffolds (Fig. 8i) as well as on the corrosion products (Fig. 8j-k).

4. Discussion

In this study, an extrusion-based 3D printing process followed by debinding and sintering was developed to fabricate porous iron scaffolds with a lay-down pattern for bone substitution. Since the biodegradation rate of bulk iron is generally too low [14,15], a geometrically ordered porous design was employed to speed up the rate of biodegradation of the specimens while maintaining the other important properties of porous iron, including its structural integrity and bone-mimicking mechanical properties. Our results showed that the lay-down pattern design, indeed, enhanced the corrosion rate of the iron scaffolds, while the bone-mimicking mechanical properties were retained. As for the cytocompatibility, the results obtained here were comparable to those reported in the other studies of porous iron [32,40,41].

4.1. Extrusion-based 3D printing and post-processing

The developed fabrication process delivered porous pure iron scaffolds with a strut size and a strut spacing close to the design values (Table 1). The use of an optimized ink formulation and ink synthesis process was of great importance for achieving such promising results. The choice of hypromellose as the binder is because of its straightforward preparation, biocompatibility [57], and its suitable rheological properties for extrusion. The iron ink was prepared with 49 vol% powder loading to strike a balance between the printability (Figure S1a-c) and the self-holding characteristics of the struts. The optimized powder-to-binder ratio demonstrated shear-thinning flow behavior (Table S1) and ensured sustainable printing without clogging in the nozzle tip and enabled the fabrication of the porous iron scaffolds with a high aspect ratio.

Following the extrusion-based 3D printing, heat treatment of the porous iron scaffolds was performed as post-processing, which started with a debinding stage where the temperature was set at a point where thermal decomposition of hypromellose took place (Figure S1d). Afterwards, the heat treatment continued to a solid-state sintering stage at a higher temperature, where iron powder particles bonded together and formed necks. The parameters of the sintering process (*i.e.*, temperature and holding time) were chosen based on the obtained solid fractions of the struts of the scaffolds under various conditions (Figure S1e). The chosen sintering temperature (1200 °C) and time (6 h) resulted in the porous iron scaffolds with an 89 ± 4% solid fraction of the struts and an absolute porosity of 67 ± 2%. It should be mentioned that a higher solid fraction can be achieved and will lead to a higher strength of the scaffolds as a result of enhanced densification [58]. However, in the case of the scaffolds intended for use as biodegradable implants, partial sintering may offer an advantage, because the scaffolds will have more exposed powder particle boundary area in the struts. Under the present sintering condition, the porous iron scaffolds possessed a pore interconnectivity of 96% (Fig. 2). It is well known that porous bone substitutes with interconnected macro- and micropores offer improved biofunctionality by favoring the adhesion, growth, and differentiation of cells during bone regeneration [59]. Due to a partial solid-state sintering process, the shrinkage of the iron scaffolds was small (*i.e.*, < 2.6%). Furthermore, under the chosen sintering condition, the iron scaffolds were only composed of the α-iron single phase (Fig. 2h), confirming the absence of any carbon residues from the decomposed polymer that could have diffused into the base material.

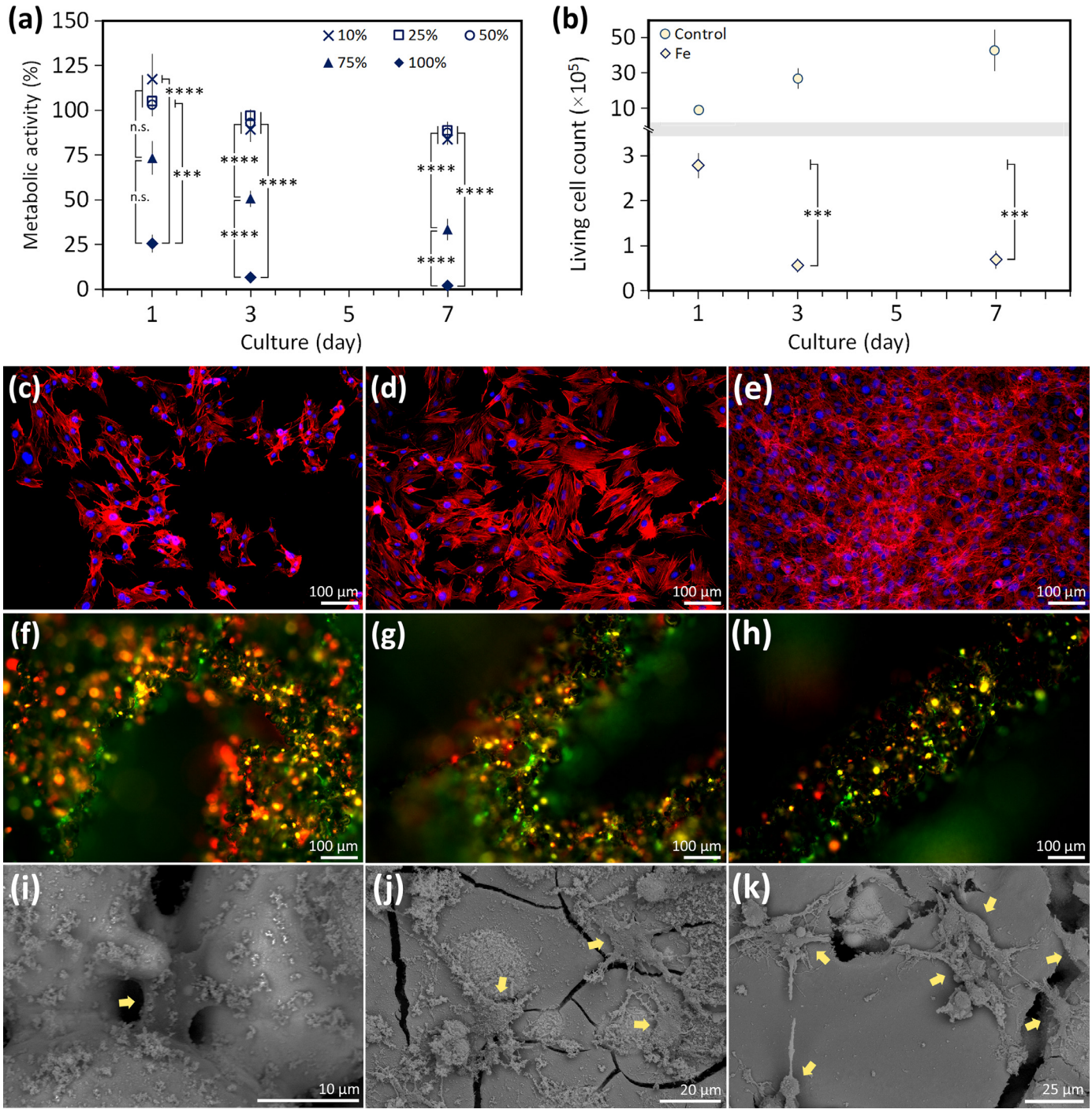

Fig. 8. *In vitro* biological evaluation of the iron scaffolds towards preosteoblasts MC3T3-E1: (a) indirect metabolic activity of preosteoblasts cultured in iron extracts for 1, 3, and 7 days, (b) the number of living preosteoblasts after 1, 3, and 7 days of direct culture on the porous iron scaffolds, (c-e) rhodamine phalloidin (red) and DAPI (blue) stained preosteoblasts after 3 days of culture in (c) 100%, (d) 75%, and (e) 50% iron extracts, (f-h) calcein acetoxymethyl (green, indicating living cells) and ethidium homodimer-1 (red, indicating dead cells) stained preosteoblasts on the scaffolds, and (i-k) the morphology of the cells after 3 days of direct cell culture on the iron scaffolds. ***, $p < 0.001$; ****, $p < 0.0001$. (For interpretation of the references to colour in this figure legend, the reader is referred to the web version of this article.)

4.2. In vitro *corrosion characteristics and mechanisms*

The static *in vitro* corrosion rate of porous iron scaffolds (0.11 ± 0.01 mg/cm^2/day at day 28) (Fig. 3f), is much higher than that of cast pure iron (*i.e.*, 0.04 – 0.06 mg/cm^2/day) [60] and that of rapidly prototyped porous iron (*i.e.*, 0.04 – 0.08 mg/cm^2/day) [32], and electrodeposited iron foam (*i.e.*, 0.023 mg/cm^2/day) [61]. The higher corrosion rate of the scaffolds was attributed to the struts that contained sintered powder particle boundaries with a micro-pore network. The random microporous interconnectivity provides many intricate sites that are favorable for autocatalytic corrosion [62–64], thereby resulting in the enhanced dissolution of iron. Furthermore, corrosion occurred not only at the periphery (Fig. 4) but also in the struts and the center of the scaffolds (Fig. 5). The penetration of the r-SBF solution into the center of the scaffolds under static immersion tests can be attributed to the capillary action in the pore network [65], thereby enhancing the corrosion of the scaffold as a whole. Nevertheless, the static *in vitro* corrosion

rate (0.05 ± 0.01 mm/year at day 28) is still lower than the pure iron with a refined grain structure, manufactured by electroforming (*i.e.*, 0.40 mm/year) [66], cross-rolling (*i.e.*, 0.11– 0.14 mm/year) [67], and selective laser melting (*i.e.*, 0.085 mm/year) [68], and thus requires an improvement to achieve an expected biodegradation rate of an ideal bone substitute (*i.e.*, 0.2 to 0.5 mm/year) [69].

When iron is exposed to a corrosive fluid, the corrosion is governed by an anodic reaction, followed by the reduction of the dissolved oxygen and water into hydroxide ions. As the corrosion proceeds, the pH of the medium increases, and iron (II, III) hydroxides form *via* the reaction of iron and hydroxide ions. Since iron (III) hydroxide is less stable, it will transform into a more stable compound, *i.e.*, iron oxide hydroxide. Moreover, due to the hypoxia condition in the incubator, the iron (II) hydroxide undergoes an anaerobic *Schikorr* reaction to form magnetite. Also, the release of iron ions increase the surrounding pH level and promote the precipitation of phosphate and bicarbonate ions from the r-SBF solution. The abovementioned corrosion reactions [68] explain the formation of iron oxide (hydroxide) and iron phosphate at the periphery (Figs. 3b and 4), as well as the presence of iron, calcium, carbon, and oxygen in the center of the scaffolds (Fig. 5) that were identified after 28 days of *in vitro* immersion.

Iron ions in the r-SBF were hardly detected by the ICP-OES analysis (Fig. 3d), due to the participation of iron ions in the formation of iron-based corrosion products that are largely insoluble in a physiological condition [40]. The release trend of iron ions was upward in the first 14 days of immersion, corresponding to the elevation of the solution pH value to 7.57. During the same period, a faster reduction of phosphate ions in the r-SBF was observed, as compared to the reduction of calcium ions. Besides the reaction with iron ions, the early period of calcium and phosphate ion reduction could also be related to the precipitation of calcium phosphate-based corrosion products (Fig. 4). Between days 14 and 28, a declining trend of iron ion release was noted. The slight increase in the pH level after 14 days of immersion may have accelerated the precipitation of iron phosphate and carbonate compounds, which explains the decreasing trends of iron ions and more consumption of calcium ions in the medium than in the first 14 days (Fig. 3d). The precipitation of iron/calcium carbonate releases hydrogen ions that balances the alkalinity of the solution. In addition, with the *in vitro* corrosion occurring in a 5% CO_2 environment, the pH of the r-SBF was also effectively maintained. The pH value slightly increased to 7.62 at the end of the immersion tests.

From the electrochemical perspective, the corrosion mechanism and kinetics of the porous iron scaffolds evolved during the immersion period (Fig. 6). The Bode impedance modulus values at the low frequency (*i.e.*, 0.01 Hz) indicates the charge transfer resistance of the material during biodegradation and at medium frequency (*i.e.*, 10 Hz) is related to the corrosion product formation [70,71]. The increasing trend of impedance modulus values at the low and medium frequencies (Figure S2c) suggests the continuous build-up of corrosion products on the iron scaffolds throughout the immersion tests [20,72]. In addition, the Bode plot of the phase angle values is indicative of the corrosion susceptibility of the material as well. A phase angle value at a high frequency (*e.g.*, at 10 kHz) close to 0°, which was observed in the specimen after 1 day of biodegradation (Fig. 6b), indicates that the material is susceptible to corrosion [73,74]. On the contrary, the phase angle shifts to a more negative value when the material exhibits more corrosion resistance, as observed for the specimens subjected to 28 days of biodegradation [73,74].

Based on the Nyquist plot after 1 day of immersion (Fig. 6c), a single arc was observed, implying the intial active corrosion of iron with a capacitive behavior [64]. The diameter of the capacitive arc indicates the corrosion rate of the material. The greater the diameter size, the slower the corrosion rate [75]. As the corrosion test progressed to day 7, the diameter of the arc increased, showing that even at the initial stage, the corrosion products hindered the progress of the corrosion process. Thereafter, between days 7 and 9, the Nyquist spectra transformed into a two-semicircle pattern (Fig. 6d). The pattern remained until 24 days of immersion. The two-semicircular arcs present in the Nyquist spectra have been reported as an indication of a corrosion mechanism that combines active and diffusive processes [76]. From the observations after 7 and 14 days of immersion, corrosion products accumulated at the periphery (Fig. 4), in the center (Fig. 5), and in the micropore network of the specimens. The active corrosion process most probably occurred on any available iron surface, while the diffusion action is expected to have taken place through the corrosion product layer that was still relatively loose and dispersed. As the corrosion advanced from day 9 to day 24 (Fig. 6d), the diameter of the arcs grew larger along with a tendency towards a more diffusive corrosion mechanism, as suggested by an increase in the arc diameter and a decreased incline slope for the lower frequencies [77]. Approaching day 28, when nearly all of the corrosion products had been turned into a dense layer, the corrosion mechanism evolved into a solely diffusion-controlled mechanism (Fig. 6e), which is hallmarked by a straight line in the Nyquist spectra in the low-frequency region [64].

From the *in vitro* immersion tests and the electrochemical analysis of the porous iron scaffolds, it is clear that the formation of the corrosion products hindered the direct dissolution of iron, hence reducing the corrosion rate over time. The evolution of the corrosion products from a loose layer to a densely structured layer during the *in vitro* immersion period is observed. This makes the long-term corrosion mechanism of porous iron scaffolds strongly dependent on the diffusion process [64]. An improvement in the corrosion rate of porous iron scaffolds can be achieved by performing dynamic *in vitro* immersion tests [41]. Although with the continuous liquid flow during *in vitro* immersion, substantial amounts of corrosion products may still adhere to the scaffolds after 28 days [41]. In an *in vivo* study on iron-based stents, a slower corrosion rate than the one estimated from the *in vitro* tests was found, due to the formation of insoluble iron-based corrosion products [78]. Therefore, the strategies to modify the corrosion products (*e.g.*, to make them less adhering) are of great interest for the further development of porous iron scaffolds as bone substitutes.

4.3. Bone-mimicking mechanical properties

For *ad interim* metallic bone scaffolds, the mechanical properties must be maintained for a certain period until the new bone tissue can take over the mechanical role of the implant and bear physiological loading. Therefore, the control over the *in vivo* degradation rate of the material is of great importance to better estimate the rate of biodegradation and avoid a sudden loss of the structural integrity of the scaffold. The mechanical properties of the porous iron scaffolds made by extrusion-based 3D printing remained in the range of those of trabecular bone (*i.e.*, E = 0.5–20 GPa and σ_y = 0.2 – 80 MPa) despite 28 days of *in vitro* biodegradation (Fig. 7) [79,80].

From the stress-strain curves, the as-sintered porous iron scaffolds (Fig. 7a) exhibited the typical mechanical characteristics of a ductile material. Unlike most geometrically ordered 3D printed porous metallic scaffolds [81,82], the stress-strain curves of the iron scaffolds did not exhibit a plateau stage. The stress-strain curves of the iron scaffolds with a 0° to 90° lay-down pattern were found to be quite similar to those of the 3D printed scaffolds designed using the solid Schwartz *p*-unit cells, which also have 90° interconnections between their struts [83,84]. In addition to the pattern, the pore network in the struts of the scaffolds acted

as the center of stress concentration. The distribution of a large number of pores in the struts can also contribute to the strain-hardening effect during plastic deformation [85], which is similar to the dispersion-strengthening effect of second-phase precipitation [86].

As an actively corroding material, the *in vitro* immersion influenced the yield strength and elastic modulus of the porous iron scaffolds (Fig. 7b). The effects of corrosion on the mechanical properties could be explained by the formation of corrosion products (Figs. 4 and 5) and a drop in the fraction of pure iron fraction in the makeup of the specimens (Fig. 5h). The interfacial bonding between iron and its corrosion products might affect the mechanical properties too [87]. Since the elastic modulus and yield strength were measured over a small range of strains during initial deformation, where loading could still be transferred across iron powder particle necks and the interfaces between iron and the corrosion products, the formation of the corrosion products led to increases in the yield strength and elastic modulus after 2 days of immersion. Afterwards, the values fluctuated throughout the 28 days of immersion but remained higher than those of the initial scaffolds. The slight increase in the yield strength and elastic modulus could be explained by considering the corrosion products as a reinforcing phase in the porous iron matrix that provided a strengthening effect. The addition of iron oxide (*i.e.*, 2 and 5 wt%) has, indeed, been reported to improve the elastic mechanical properties of the iron-iron oxide composite [88]. The fluctuations in the yield strength and elastic modulus over the immersion time may be due to the evolution of the corrosion product morphology that influenced their interfacial bonding with the specimens. Another relevant factor could be the decreasing fraction of iron in the scaffolds as corrosion progressed. The latter would significantly affect the ductility of the scaffolds (Fig. 7c).

4.4. Cytocompatibility characteristics

Different levels of preosteoblast viability (Fig. 8a) were observed depending on the dilution level of the iron extract. According to the ISO 10993-5 [89], the 100% iron extract was severely toxic (level 4) with nearly no metabolically active cells. The 75% iron extract was categorized as moderately toxic (level 3) with more than 50% growth inhibition, while the iron extracts $\leq$ 50% were slightly toxic (level 1) with more than 80% metabolic activity even after 7 days of culture. Moreover, the rhodamine-phalloidin and DAPI staining (Fig. 8c-e) clearly showed the unfavorable effects of undiluted extracts on the growth of the preosteoblasts. The number of cells increased in the diluted extracts contributing to the higher metabolic activity detected. The cytotoxicity of iron is often related to the uncontrolled formation of ROS, including superoxide anions and hydroxyl radicals *via* the Fenton reactions [90]. Although a proper ROS level plays an important part in some biological events, such as the activation of signaling pathways and gene expression, excessive ROS may lead to oxidative stresses, which will harm the cells [90].

Of note, the iron extracts were prepared with an extraction ratio of 5 cm^2/mL, which is higher than the most reported extraction ratios in the *in vitro* studies of iron-based materials (*e.g.*, 2.5 cm^2/mL [32] and 1.25 cm^2/mL [43,68,91]). In addition to the relatively high solution volume-to-surface area ratio, the 72 h iron extraction in the cell culture medium resulted in a higher iron ion concentration as compared to the extract from the r-SBF medium, which is most likely due to the presence of serum [92,93]. A higher extraction ratio combined with a high iron ion release of the scaffolds created in this study explains the immediate cytotoxicity of the 100% iron extract that was observed. A safe iron ion concentration for bone marrow stem cells has been reported to be $<$ 75 mg/L [13], which is similar to the results obtained in our extraction-based assays with $\leq$ 50% iron extracts and the other results obtained from indirect cell culture [32,43,68,91]. Most *in vivo* studies on iron-based materials for implant applications have found those biomaterials to be systemically biocompatible [14,94–96], while only a few studies have found some evidence of local inflammation post implantation [95,96]. In our indirect assays, the more cytocompatible iron extracts (*i.e.*, $\leq$ 50%) are more likely to correspond to the actual *in vivo* conditions, given the fact that the dynamic flow of body fluids will inevitably decrease the concentration of iron ions in the implant vicinity. Given the high baseline of iron loading in the blood (*i.e.*, 0.447 g/L), the release of iron ions from an implant is too small to cause systemic toxicity [97]. Local tissue toxicity analysis is, therefore, more relevant for such porous iron.

The present direct cell seeding tests demonstrated a cytotoxic effect of the porous iron scaffolds with a 17-fold reduction of viable cells within the first 3 days of culture, and afterwards only growth inhibition. Reductions in cell viability were also observed in the direct culture of mouse bone marrow stem cells on 60 vol% porous Fe-30Mn scaffolds [31], human osteosarcoma cells on 40 vol% porous Fe-30Mn6Si1Pd scaffolds [29], 3T3 fibroblasts [32] as well as rabbit bone marrow stem cells [35] on porous iron scaffolds. Interestingly, despite significant reductions in the number of viable cells, the preosteoblasts were still found stretching in the pores (Fig. 8i) and adhering to the corrosion products of the porous iron scaffolds (Fig. 8j-k). The spreading morphology of the preosteoblasts may be due to the combined effect of the surface morphology and the presence of calcium- and phosphate-based corrosion products that are known to be osteoconductive [14]. Since *in vitro* cytocompatibility assessment cannot completely mimic the *in vivo* conditions, these preliminary results warrant *in vivo* studies on 3D printed porous iron scaffolds, particularly to study the local cyto- and histo-compatibility of the porous iron scaffolds.

5. Conclusions

In this study, the iron scaffolds with a lay-down pattern were successfully fabricated by using extrusion-based 3D printing and subsequent sintering, which allowed for comprehensive characterization of the material for application as a biodegradable bone substitute. The structure of the fabricated porous iron scaffolds was highly interconnected, owing to the presence of macropores from the pattern design and random micropores in the struts. After 28 days of static *in vitro* immersion, the mass of the porous iron reduced by 7%. The *in vitro* corrosion rate decreased from 0.28 down to 0.11 mg/cm^2/day, with different corrosion mechanisms operating over the 28 days of static immersion. The yield strength and elastic modulus of the porous iron scaffolds slightly increased due to the formation of corrosion products in the struts during the 28 days of *in vitro* corrosion. These values remained within the range of the mechanical properties of trabecular bone. The direct culture of preosteoblasts on the iron scaffolds revealed cytotoxicity, due to the high concentration of iron ions, as explained by the results from the extraction-based assays. Further *in vitro* cytotoxicity experiments (*e.g.*, co-culture of multiple types of cells and *in vivo* studies) should be performed [84] under dynamic conditions. Taken together, our results showed that extrusion-based 3D printing could deliver porous iron scaffolds with enhanced biodegradability and bone-mimicking mechanical properties for potential application as bone substitutes. Introducing bioactive components in the form of coatings [15] or inside the scaffold body to form composites [36,69] may be explored to further improve the biofunctionalities of such 3D printed porous iron scaffolds.

Declaration of Competing Interest

The authors declare that they have no known competing financial interests or personal relationships that could have appeared to influence the work reported in this paper.

Acknowledgments

This work is part of the 3DMed project that has received the funding from the Interreg 2 Seas program 2014 – 2020, co-funded by the European Regional Development Fund under subsidy contract no. 2S04-014. Mr. Ruud Hendrikx at the Department of Materials Science and Engineering, Delft University of Technology, is acknowledged for the XRD analysis. Mr. Michel van den Brink at the Department of Process and Energy, Delft University of Technology, is acknowledged for the ICP-OES analysis. The authors thank Ms. Agnieszka Kooijman at the Department of Materials Science and Engineering, Delft University of Technology for the assistance in the electrochemical experiments.

Supplementary materials

Supplementary material associated with this article can be found, in the online version, at doi:10.1016/j.actbio.2020.11.022.

References

[1] H. Hermawan, Updates on the research and development of absorbable metals for biomedical applications, Prog. Biomater. 7 (2018) 93–110, doi:10.1007/s40204-018-0091-4.
[2] H.S. Han, S. Loffredo, I. Jun, J. Edwards, Y.C. Kim, H.K. Seok, F. Witte, D. Mantovani, S. Glyn-Jones, Current status and outlook on the clinical translation of biodegradable metals, Mater. Today. 23 (2019) 57–71, doi:10.1016/j.mattod.2018.05.018.
[3] Y.F. Zheng, X.N. Gu, F. Witte, Biodegradable metals, Mater. Sci. Eng. R. 77 (2014) 1–34, doi:10.1007/978-1-4614-3942-4_5.
[4] M. Schinhammer, A.C. Hänzi, J.F. Löffler, P.J. Uggowitzer, Design strategy for biodegradable Fe-based alloys for medical applications, Acta Biomater. 6 (2010) 1705–1713, doi:10.1016/j.actbio.2009.07.039.
[5] J. He, F.L. He, D.W. Li, Y.L. Liu, Y.Y. Liu, Y.J. Ye, D.C. Yin, Advances in Fe-based biodegradable metallic materials, RSC Adv. 6 (2016) 112819–112838, doi:10.1039/C6RA20594A.
[6] R. Gorejová, L. Haverová, R. Oriňaková, A. Oriňak, M. Oriňak, Recent advancements in Fe-based biodegradable materials for bone repair, J. Mater. Sci. 54 (2019) 1913–1947, doi:10.1007/s10853-018-3011-z.
[7] N. Abbaspour, R. Hurrell, R. Kelishadi, Review on iron and its importance for human health, J. Res. Med. Sci. (2014).
[8] E. Balogh, G. Paragh, V. Jeney, Influence of iron on bone homeostasis, Pharmaceuticals 11 (2018) 1–18, doi:10.3390/ph11040107.
[9] F. Atashi, A. Modarressi, M.S. Pepper, The role of reactive oxygen species in mesenchymal stem cell adipogenic and osteogenic differentiation: a review, Stem Cells Dev. 24 (2015) 1150–1163, doi:10.1089/scd.2014.0484.
[10] M. Parelman, B. Stoecker, A. Baker, D. Medeiros, Iron restriction negatively affects bone in female rats and mineralization of hFOB osteoblast cells, Exp. Biol. Med. 231 (2006) 378–386, doi:10.1177/153537020623100403.
[11] J.G. Messer, P.T. Cooney, D.E. Kipp, Iron chelator deferoxamine alters iron-regulatory genes and proteins and suppresses osteoblast phenotype in fetal rat calvaria cells, Bone 46 (2010) 1408–1415, doi:10.1016/j.bone.2010.01.376.
[12] D. Praticò, M. Pasin, O.P. Barry, A. Ghiselli, G. Sabatino, L. Iuliano, G.A. Fitzgerald, F. Violi, Iron-dependent human platelet activation and hydroxyl radical formation: involvement of protein kinase C, Circulation (1999), doi:10.1161/01.CIR.99.24.3118.
[13] E. Zhang, H. Chen, F. Shen, Biocorrosion properties and blood and cell compatibility of pure iron as a biodegradable biomaterial, J. Mater. Sci. Mater. Med. 21 (2010) 2151–2163, doi:10.1007/s10856-010-4070-0.
[14] T. Kraus, F. Moszner, S. Fischerauer, M. Fiedler, E. Martinelli, J. Eichler, F. Witte, E. Willbold, M. Schinhammer, M. Meischel, P.J. Uggowitzer, J.F. Löffler, A. Weinberg, Biodegradable Fe-based alloys for use in osteosynthesis: outcome of an *in vivo* study after 52 weeks, Acta Biomater 10 (2014) 3346–3353, doi:10.1016/j.actbio.2014.04.007.
[15] S. Ray, U. Thormann, M. Eichelroth, M. Budak, C. Biehl, M. Rupp, U. Sommer, T. El Khassawna, F.I. Alagboso, M. Kampschulte, M. Rohnke, A. Henß, K. Peppler, V. Linke, P. Quadbeck, A. Voigt, F. Stenger, D. Karl, R. Schnettler, C. Heiss, K.S. Lips, V. Alt, Strontium and bisphosphonate coated iron foam scaffolds for osteoporotic fracture defect healing, Biomaterials 157 (2018) 1–16, doi:10.1016/j.biomaterials.2017.11.049.
[16] M.H. Emily Walker, Magnesium, iron and zinc alloys, the trifecta of bioresorbable orthopaedic and vascular implantation - a review, J. Biotechnol. Biomater. (2015), doi:10.4172/2155-952x.1000178.
[17] Y. Ishikawa, Y. Endoh, Antiferromagnetism of γ-FeMn alloys, J. Appl. Phys. 39 (1968) 1318–1319, doi:10.1063/1.1656274.
[18] Y.P. Feng, A. Blanquer, J. Fornell, H. Zhang, P. Solsona, M.D. Baró, S. Suriñach, E. Ibáñez, E. García-Lecina, X. Wei, R. Li, L. Barrios, E. Pellicer, C. Nogues, J. Sort, Novel Fe-Mn-Si-Pd alloys: insights into mechanical, magnetic, corrosion resistance and biocompatibility performances, R, Soc. Chem. 4 (2016) 6402–6412, doi:10.1039/c6tb01951j.
[19] J. Hufenbach, H. Wendrock, F. Kochta, U. Kühn, A. Gebert, Novel biodegradable Fe-Mn-C-S alloy with superior mechanical and corrosion properties, Mater. Lett. 186 (2017) 330–333, doi:10.1016/j.matlet.2016.10.037.
[20] J. Zhou, Y. Yang, M. Alonso Frank, R. Detsch, A.R. Boccaccini, S. Virtanen, Accelerated degradation behavior and cytocompatibility of pure iron treated with sandblasting, ACS Appl. Mater. Interfaces 8 (2016) 26482–26492, doi:10.1021/acsami.6b07068.
[21] A.H.M. Yusop, N.M. Daud, H. Nur, M.R.A. Kadir, H. Hermawan, Controlling the degradation kinetics of porous iron by poly(lactic-co-glycolic acid) infiltration for use as temporary medical implants, Sci. Rep. 5 (2015) 1–17, doi:10.1038/srep11194.
[22] L. Haverová, R. Oriňaková, A. Oriňak, R. Gorejová, M. Baláž, P. Vanýsek, M. Kupková, M. Hrubovčáková, P. Mudroň, J. Radoňák, Z.O. Králová, A.M. Turoňová, An *in vitro* corrosion study of open cell iron structures with PEG coating for bone replacement applications, Metals (Basel) 8 (2018) 1–21, doi:10.3390/met8070499.
[23] R. Gorejová, R. Oriňaková, Z. Orságová Králová, M. Baláž, M. Kupková, M. Hrubovčáková, L. Haverová, M. Džupon, A. Oriňak, F. Kaľavský, K. Kovaľ, *In vitro* corrosion behavior of biodegradable iron foams with polymeric coating, Materials (Basel) 13 (2020) 1–17.
[24] Y. Su, S. Champagne, A. Trenggono, R. Tolouei, D. Mantovani, H. Hermawan, Development and characterization of silver containing calcium phosphate coatings on pure iron foam intended for bone scaffold applications, Mater. Des. 148 (2018) 124–134, doi:10.1016/j.matdes.2018.03.061.
[25] J. He, H. Ye, Y. Li, J. Fang, Q. Mei, X. Lu, F. Ren, Cancellous-bone-like porous iron scaffold coated with strontium incorporated octacalcium phosphate nanowhiskers for bone regeneration, ACS Biomater. Sci. Eng. 5 (2019) 509–518, doi:10.1021/acsbiomaterials.8b01188.
[26] R. Alavi, A. Trenggono, S. Champagne, H. Hermawan, Investigation on mechanical behavior of biodegradable iron foams under different compression test conditions, Metals (Basel) 7 (2017) 202, doi:10.3390/met7060202.
[27] J. Čapek, D. Vojtěch, Microstructural and mechanical characteristics of porous iron prepared by powder metallurgy, Mater. Sci. Eng. C. 43 (2014) 494–501, doi:10.1016/j.msec.2014.06.046.
[28] J. Čapek, D. Vojtěch, A. Oborná, Microstructural and mechanical properties of biodegradable iron foam prepared by powder metallurgy, Mater. Des. 83 (2015) 468–482, doi:10.1016/j.matdes.2015.06.022.
[29] Y.P. Feng, N. Gaztelumendi, J. Fornell, H.Y. Zhang, P. Solsona, M.D. Baró, S. Suriñach, E. Ibáñez, L. Barrios, E. Pellicer, C. Nogués, J. Sort, Mechanical properties, corrosion performance and cell viability studies on newly developed porous Fe-Mn-Si-Pd alloys, J. Alloys Compd. 724 (2017) 1046–1056, doi:10.1016/j.jallcom.2017.07.112.
[30] M. Heiden, E. Nauman, L. Stanciu, Bioresorbable Fe–Mn and Fe–Mn–HA m for orthopedic implantation: enhancing degradation through porosity control, Adv. Healthc. Mater. 6 (2017) 1–12, doi:10.1002/adhm.201700120.
[31] S.M. Huang, E.A. Nauman, L.A. Stanciu, Investigation of porosity on mechanical properties, degradation and in-vitro cytotoxicity limit of Fe30Mn using space holder technique, Mater. Sci. Eng. C. 99 (2019) 1048–1057, doi:10.1016/j.msec.2019.02.055.
[32] P. Sharma, K.G. Jain, P.M. Pandey, S. Mohanty, *In vitro* degradation behaviour, cytocompatibility and hemocompatibility of topologically ordered porous iron scaffold prepared using 3D printing and pressureless microwave sintering, Mater. Sci. Eng. C. 106 (2020) 110247, doi:10.1016/j.msec.2019.110247.
[33] D.T. Chou, D. Wells, D. Hong, B. Lee, H. Kuhn, P.N. Kumta, Novel processing of iron-manganese alloy-based biomaterials by inkjet 3-D printing, Acta Biomater. 9 (2013) 8593–8603, doi:10.1016/j.actbio.2013.04.016.
[34] D. Hong, D.T. Chou, O.I. Velikokhatnyi, A. Roy, B. Lee, I. Swink, I. Issaev, H.A. Kuhn, P.N. Kumta, Binder-jetting 3D printing and alloy development of new biodegradable Fe-Mn-Ca/Mg alloys, Acta Biomater. 45 (2016) 375–386, doi:10.1016/j.actbio.2016.08.032.
[35] C. Yang, Z. Huan, X. Wang, C. Wu, J. Chang, 3D printed Fe scaffolds with HA nanocoating for bone regeneration, ACS Biomater. Sci. Eng. 4 (2018) 608–616, doi:10.1021/acsbiomaterials.7b00885.
[36] H. Ma, T. Li, Z. Huan, M. Zhang, Z. Yang, J. Wang, J. Chang, C. Wu, 3D printing of high-strength bioscaffolds for the synergistic treatment of bone cancer, NPG Asia Mater 10 (2018) 31–44, doi:10.1038/s41427-018-0015-8.
[37] D.K. Mishra, P.M. Pandey, Experimental investigation into the fabrication of green body developed by micro-extrusion-based 3D printing process, Polym. Compos. 41 (2020) 1986–2002, doi:10.1002/pc.25514.
[38] D.K. Mishra, P.M. Pandey, Effect of sintering parameters on the microstructure and compressive mechanical properties of porous Fe scaffold fabricated using 3D printing and pressure less microwave sintering, Proc. Inst. Mech. Eng. Part C J. Mech. Eng. Sci. 0 (2020) 1–16, doi:10.1177/0954406220921416.
[39] D.K. Mishra, P.M. Pandey, Mechanical behaviour of 3D printed ordered pore topological iron scaffold, Mater. Sci. Eng. A. 783 (2020) 139293, doi:10.1016/j.msea.2020.139293.

[40] Y. Li, H. Jahr, K. Lietaert, P. Pavanram, A. Yilmaz, L.I. Fockaert, M.A. Leeflang, B. Pouran, Y. Gonzalez-Garcia, H. Weinans, J.M.C. Mol, J. Zhou, A.A. Zadpoor, Additively manufactured biodegradable porous iron, Acta Biomater. 77 (2018) 380–393, doi:10.1016/j.actbio.2018.07.011.
[41] Y. Li, H. Jahr, P. Pavanram, F.S.L. Bobbert, U. Puggi, X.Y. Zhang, B. Pouran, M.A. Leeflang, H. Weinans, J. Zhou, A.A. Zadpoor, Additively manufactured functionally graded biodegradable porous iron, Acta Biomater. 96 (2019) 646–661, doi:10.1016/j.actbio.2019.07.013.
[42] C. Shuai, W. Yang, Y. Yang, H. Pan, C. He, F. Qi, D. Xie, H. Liang, Selective laser melted Fe-Mn bone scaffold: microstructure, corrosion behavior and cell response, Mater. Res. Express. 7 (2019).
[43] D. Carluccio, C. Xu, J. Venezuela, Y. Cao, D. Kent, M. Bermingham, A.G. Demir, B. Previtali, Q. Ye, M. Dargusch, Additively manufactured iron-manganese for biodegradable porous load-bearing bone scaffold applications, Acta Biomater. 103 (2020) 346–360, doi:10.1016/j.actbio.2019.12.018.
[44] A.A. Zadpoor, J. Malda, Additive manufacturing of biomaterials, tissues, and organs, Ann. Biomed. Eng. 45 (2017) 1–11, doi:10.1007/s10439-016-1719-y.
[45] Y. Qin, P. Wen, H. Guo, D. Xia, Y. Zheng, L. Jauer, R. Poprawe, M. Voshage, J. Henrich, Additive manufacturing of biodegradable metals: current research status and future perspectives, Acta Biomater. (2019), doi:10.1016/j.actbio.2019.04.046.
[46] N.E. Putra, M.J. Mirzaali, I. Apachitei, J. Zhou, A.A. Zadpoor, Multi-material additive manufacturing technologies for Ti-, Mg-, and Fe-based biomaterials for bone substitution, Acta Biomater. (2020), doi:10.1016/j.actbio.2020.03.037.
[47] C. Shuai, G. Liu, Y. Yang, F. Qi, S. Peng, W. Yang, C. He, G. Wang, G. Qian, A strawberry-like Ag-decorated barium titanate enhances piezoelectric and antibacterial activities of polymer scaffold, Nano Energy (2020), doi:10.1016/j.nanoen.2020.104825.
[48] Y. Yang, C. Lu, S. Peng, L. Shen, D. Wang, F. Qi, C. Shuai, Laser additive manufacturing of Mg-based composite with improved degradation behaviour, Virtual Phys. Prototyp. (2020), doi:10.1080/17452759.2020.1748381.
[49] ASTM B963-17Standard Test Methods For Oil content, Oil-Impregnation efficiency, and Surface-Connected Porosity of Sintered Powder Metallurgy (PM) Products Using Archimedes' Principle, ASTM International, 2017, doi:10.1520/B0963-14.
[50] A. Oyane, H. Kim, T. Furuya, T. Kokubo, T. Miyazaki, T. Nakamura, Preparation and assessment of revised simulated body fluids, J. Biomed. Mater. Res. - Part A. (2003) 188–195, doi:10.1093/toxsci/16.3.401.
[51] L. Yang, E. Zhang, Biocorrosion behavior of magnesium alloy in different simulated fluids for biomedical application, Mater. Sci. Eng. C. 29 (2009) 1691–1696, doi:10.1016/j.msec.2009.01.014.
[52] ASTM G1-03Standard Practice For preparing, cleaning, and Evaluating Corrosion Test, ASTM International, 2017, doi:10.1520/G0001-03R11.
[53] ASTM G31-72Standard Practice For Laboratory Immersion Corrosion Testing For Metals, ASTM International, 2004, doi:10.1520/G0031-72R04.
[54] ASTM G102-89Standard Practice For Calculation of Corrosion Rates and Related Information from Electrochemical Measurements, ASTM International, 2015, doi:10.1520/G0102-89R15E01.
[55] ISO 13314Mechanical Testing of Metals - Ductility testing - Compression test For Porous and Cellular Metals, International Organization for Standardization, 2011 ISO 13314:2011.
[56] ISO 10993-12Sample Preparation and Reference Materials, International Organization for Standardization, 2012, doi:10.1016/S0080-8784(08)60069-1.
[57] C.L. Li, L.G. Martini, J.L. Ford, M. Roberts, The use of hypromellose in oral drug delivery, J. Pharm. Pharmacol. (2005), doi:10.1211/0022357055957.
[58] I. Rishmawi, M. Salarian, M. Vlasea, Tailoring green and sintered density of pure iron parts using binder jetting additive manufacturing, Addit. Manuf. 24 (2018) 508–520, doi:10.1016/j.addma.2018.10.015.
[59] J.M. Seok, T. Rajangam, J.E. Jeong, S. Cheong, S.M. Joo, S.J. Oh, H. Shin, S.H. Kim, S.A. Park, Fabrication of 3D plotted scaffold with microporous strands for bone tissue engineering, J. Mater. Chem. B. 8 (2020) 951–960, doi:10.1039/c9tb02360g.
[60] T. Huang, J. Cheng, Y.F. Zheng, *In vitro* degradation and biocompatibility of Fe-Pd and Fe-Pt composites fabricated by spark plasma sintering, Mater. Sci. Eng. C. 35 (2014) 43–53, doi:10.1016/j.msec.2013.10.023.
[61] J. He, F.L. He, D.W. Li, Y.L. Liu, D.C. Yin, A novel porous Fe/Fe-W alloy scaffold with a double-layer structured skeleton: preparation, *in vitro* degradability and biocompatibility, Colloids Surf. B Biointerface. 142 (2016) 325–333, doi:10.1016/j.colsurfb.2016.03.002.
[62] F. Xie, X. He, S. Cao, M. Mei, X. Qu, Influence of pore characteristics on microstructure, mechanical properties and corrosion resistance of selective laser sintered porous Ti-Mo alloys for biomedical applications, Electrochim. Acta. (2013), doi:10.1016/j.electacta.2013.04.105.
[63] E. Aghion, Y. Perez, Effects of porosity on corrosion resistance of Mg alloy foam produced by powder metallurgy technology, Mater. Charact. (2014), doi:10.1016/j.matchar.2014.07.012.
[64] P. Sharma, P.M. Pandey, Corrosion behaviour of the porous iron scaffold in simulated body fluid for biodegradable implant application, Mater. Sci. Eng. C. 99 (2019) 838–852, doi:10.1016/j.msec.2019.01.114.
[65] D.S. Oh, Y.J. Kim, M.H. Hong, M.H. Han, K. Kim, Effect of capillary action on bone regeneration in micro-channeled ceramic scaffolds, Ceram. Int. (2014), doi:10.1016/j.ceramint.2014.02.033.
[66] M. Moravej, A. Purnama, M. Fiset, J. Couet, D. Mantovani, Electroformed pure iron as a new biomaterial for degradable stents: *in vitro* degradation and preliminary cell viability studies, Acta Biomater. 6 (2010) 1843–1851, doi:10.1016/j.actbio.2010.01.008.
[67] C.S. Obayi, R. Tolouei, C. Paternoster, S. Turgeon, B.A. Okorie, D.O. Obikwelu, G. Cassar, J. Buhagiar, D. Mantovani, Influence of cross-rolling on the microtexture and biodegradation of pure iron as biodegradable material for medical implants, Acta Biomater. 17 (2015) 68–77, doi:10.1016/j.actbio.2015.01.024.
[68] C. Shuai, S. Li, G. Wang, Y. Yang, S. Peng, C. Gao, Strong corrosion induced by carbon nanotubes to accelerate Fe biodegradation, Mater. Sci. Eng. C. 104 (2019) 109935, doi:10.1016/j.msec.2019.109935.
[69] C. Gao, M. Yao, S. Li, P. Feng, S. Peng, C. Shuai, Highly biodegradable and bioactive Fe-Pd-bredigite biocomposites prepared by selective laser melting, J. Adv. Res. 20 (2019) 91–104, doi:10.1016/j.jare.2019.06.001.
[70] C. Valero, A. Igual, Electrochemical aspects in biomedical alloy characterization: electrochemical Impedance Spectrosopy, Biomed. Eng. Trends Mater. Sci. (2011), doi:10.5772/13039.
[71] J. Tedim, M.L. Zheludkevich, A.C. Bastos, A.N. Salak, A.D. Lisenkov, M.G.S. Ferreira, Influence of preparation conditions of Layered Double Hydroxide conversion films on corrosion protection, Electrochim. Acta. (2014), doi:10.1016/j.electacta.2013.11.111.
[72] A. Xu, F. Zhang, F. Jin, R. Zhang, B. Luo, T. Zhang, The evaluation of coating performance by analyzing the intersection of Bode plots, Int. J. Electrochem. Sci. (2014).
[73] M. Mahdavian, M.M. Attar, Another approach in analysis of paint coatings with EIS measurement: phase angle at high frequencies, Corros. Sci. (2006), doi:10.1016/j.corsci.2006.03.012.
[74] Y. Zuo, R. Pang, W. Li, J.P. Xiong, Y.M. Tang, The evaluation of coating performance by the variations of phase angles in middle and high frequency domains of EIS, Corros. Sci. (2008), doi:10.1016/j.corsci.2008.08.049.
[75] X. Liu, S. Chen, H. Ma, G. Liu, L. Shen, Protection of iron corrosion by stearic acid and stearic imidazoline self-assembled monolayers, Appl. Surf. Sci. (2006), doi:10.1016/j.apsusc.2006.01.038.
[76] D. You, N. Pebere, F. Dabosi, An investigation of the corrosion of pure iron by electrochemical techniques and *in situ* observations, Corros. Sci. (1993), doi:10.1016/0010-938X(93)90254-E.
[77] B.A. Mei, O. Munteshari, J. Lau, B. Dunn, L. Pilon, Physical Interpretations of Nyquist Plots for EDLC Electrodes and Devices, J. Phys. Chem. C. (2018), doi:10.1021/acs.jpcc.7b10582.
[78] A. Drynda, T. Hassel, F.W. Bach, M. Peuster, *In vitro* and *in vivo* corrosion properties of new iron-manganese alloys designed for cardiovascular applications, J. Biomed. Mater. Res. - Part B Appl. Biomater. 103 (2015) 649–660, doi:10.1002/jbm.b.33234.
[79] T.M. Keaveny, W.C. Hayes, Mechanical properties of cortical and trabecular bone, Bone 7 (1993) 285–344.
[80] T.M. Keaveny, E.F. Morgan, G.L. Niebur, O.C. Yeh, Biomechanics of trabecular bone, Annu. Rev. Biomed. Eng. 3 (2001) 307–333.
[81] S.M. Ahmadi, S.A. Yavari, R. Wauthle, B. Pouran, J. Schrooten, H. Weinans, A.A. Zadpoor, Additively manufactured open-cell porous biomaterials made from six different space-filling unit cells: the mechanical and morphological properties, Materials (Basel) (2015), doi:10.3390/ma8041871.
[82] F.S.L. Bobbert, K. Lietaert, A.A. Eftekhari, B. Pouran, S.M. Ahmadi, H. Weinans, A.A. Zadpoor, Additively manufactured metallic porous biomaterials based on minimal surfaces: a unique combination of topological, mechanical, and mass transport properties, Acta Biomater. (2017), doi:10.1016/j.actbio.2017.02.024.
[83] N. Soro, H. Attar, X. Wu, M.S. Dargusch, Investigation of the structure and mechanical properties of additively manufactured Ti-6Al-4 V biomedical scaffolds designed with a Schwartz primitive unit-cell, Mater. Sci. Eng. A. (2019), doi:10.1016/j.msea.2018.12.104.
[84] D. Carluccio, C. Xu, J. Venezuela, Y. Cao, D. Kent, M. Bermingham, A.G. Demir, B. Previtali, Q. Ye, M. Dargusch, Additively manufactured iron-manganese for biodegradable porous load-bearing bone scaffold applications, (2019) 1–15. 10.1016/j.actbio.2019.12.018.
[85] Y.N. Podrezov, L.G. Shtyka, D.G. Verbylo, Strain hardening of porous iron under uniaxial compression, Powder Metall. Met. Ceram. (2000), doi:10.1007/BF02677449.
[86] G. Cui, X. Wei, E.A. Olevsky, R.M. German, J. Chen, The manufacturing of high porosity iron with an ultra-fine microstructure via free pressureless spark plasma sintering, Materials (Basel) 9 (2016) 1–9, doi:10.3390/ma9060495.
[87] S.Y. Fu, X.Q. Feng, B. Lauke, Y.W. Mai, Effects of particle size, particle/matrix interface adhesion and particle loading on mechanical properties of particulate-polymer composites, Compos. Part B Eng. (2008), doi:10.1016/j.compositesb.2008.01.002.
[88] J. Cheng, T. Huang, Y.F. Zheng, Microstructure, mechanical property, biodegradation behavior, and biocompatibility of biodegradable Fe-Fe2O3 composites, J. Biomed. Mater. Res. - Part A. 102 (2014) 2277–2287, doi:10.1002/jbm.a.34882.
[89] ISO 10993-5Tests For *in Vitro* Cytotoxicity, International Organization for Standardization, 2009, doi:10.1021/es0620181.
[90] Y.F. He, Y. Ma, C. Gao, G.Y. Zhao, L.L. Zhang, G.F. Li, Y.Z. Pan, K. Li, Y.J. Xu, Iron overload inhibits osteoblast biological activity through oxidative stress, Biol. Trace Elem. Res. (2013), doi:10.1007/s12011-013-9605-z.
[91] M.S. Dargusch, A. Dehghan-Manshadi, M. Shahbazi, J. Venezuela, X. Tran, J. Song, N. Liu, C. Xu, Q. Ye, C. Wen, Exploring the role of manganese on the microstructure, mechanical properties, biodegradability, and biocompatibility of porous iron-based scaffolds, ACS Biomater. Sci. Eng. 5 (2019) 1686–1702, doi:10.1021/acsbiomaterials.8b01497.
[92] V. Wagener, A.S. Faltz, M.S. Killian, P. Schmuki, S. Virtanen, Protein interactions with corroding metal surfaces: comparison of Mg and Fe, Faraday Discuss. (2015), doi:10.1039/c4fd00253a.

[93] R. Oriňaková, R. Gorejová, Z.O. Králová, A. Oriňak, I. Shepa, J. Hovancová, A. Kovalčíková, Z.L. Bujňáková, N. Király, M. Kaňuchová, M. Baláž, M. Strečková, M. Kupková, M. Hrubovčáková, F. Kaľavský, M. Oriňak, Influence of albumin interaction on corrosion resistance of sintered iron biomaterials with polyethyleneimine coating, Appl. Surf. Sci. (2020), doi:10.1016/j.apsusc.2020.145379.

[94] M. Fântânariu, L.C. Trinc, C. Solcan, A. Trofin, E.V. S, S. Stanciu, A new Fe-Mn-Si alloplastic biomaterial as bone grafting material: *in vivo* study, Appl. Surf. Sci. 352 (2015) 129–139, doi:10.1016/j.apsusc.2015.04.197.

[95] Q. Feng, D. Zhang, C. Xin, X. Liu, W. Lin, W. Zhang, S. Chen, K. Sun, Characterization and *in vivo* evaluation of a bio-corrodible nitrided iron stent, J. Mater. Sci. Mater. Med. (2013), doi:10.1007/s10856-012-4823-z.

[96] M. Traverson, M. Heiden, L.A. Stanciu, E.A. Nauman, Y. Jones-hall, G.J. Breur, *In vivo* evaluation of biodegradability and biocompatibility of Fe30Mn alloy, Vet. Comp. Orthop. Traumatol. 31 (2018) 10–16.

[97] E. Scarcello, D. Lison, Are Fe-based stenting materials biocompatible? A critical review of *in vitro* and *in vivo* studies, J. Funct. Biomater. (2020), doi:10.3390/jfb11010002.